Monthly Notices
of the
ROYAL ASTRONOMICAL SOCIETY

Mon. Not. R. Astron. Soc. **413,** 80–100 (2011) doi:10.1111/j.1365-2966.2010.18113.x

The *Hubble Space Telescope* GOODS NICMOS Survey: overview and the evolution of massive galaxies at $1.5 < z < 3$

C. J. Conselice,[1⋆] A. F. L. Bluck,[1] F. Buitrago,[1] A. E. Bauer,[1] R. Grützbauch,[1] R. J. Bouwens,[2,3] S. Bevan,[1] A. Mortlock,[1] M. Dickinson,[4] E. Daddi,[5] H. Yan,[6] Douglas Scott,[7] S. C. Chapman,[8] R.-R. Chary,[9] H. C. Ferguson,[10] M. Giavalisco,[11] N. Grogin,[10] G. Illingworth,[2] S. Jogee,[12] A. M. Koekemoer,[10] Ray A. Lucas,[10] B. Mobasher,[13] L. Moustakas,[14] C. Papovich,[15] S. Ravindranath,[16] B. Siana,[17] H. Teplitz,[18] I. Trujillo,[19] M. Urry[20] and T. Weinzirl[12]

[1]*University of Nottingham, School of Physics & Astronomy, Nottingham NG7 2RD*
[2]*Lick Observatory, University of California, Santa Cruz, CA 95064, USA*
[3]*Leiden Observatory, Leiden University, NL-2300 RA Leiden, Netherlands*
[4]*National Optical Astronomical Observatories, Tucson, AZ 85719, USA*
[5]*CEA/DSM-CNRS, CEA Saclay, Bât 141, Gif-sur-Yvette, Cedex, F-91191, France*
[6]*Ohio State University, Department of Astronomy, 140 W. 18th Avenue, Columbus, OH 43210-1173, USA*
[7]*Department of Physics & Astronomy, University of British Columbia, Vancouver, BC, V6T 1Z1, Canada*
[8]*Institute of Astronomy, Cambridge University, Madingley Road, Cambridge CB3 0HA*
[9]*Spitzer Science Center, California Institute of Technology, Pasadena, CA 91125, USA*
[10]*Space Telescope Science Institute, 3700 San Martin Drive, Baltimore, MD 21218, USA*
[11]*Department of Astronomy, University of Massachuetts, Amherst, MA 01003-9305, USA*
[12]*Department of Astronomy, University of Texas, Austin, TX 78712-1021, USA*
[13]*Department of Physics & Astronomy, University of California, Riverside, CA 92521, USA*
[14]*Jet Propulsion Laboratory, California Institute of Technology, Pasadena, CA 91109, USA*
[15]*Department of Physics & Astronomy, Texas A&M University, College Station, TX 77843-4242, USA*
[16]*IUCAA, Pune University Campus, Pune 411007, Maharashtra, India*
[17]*Astronomy Department, California Institute of Technology, MC 105-24, Pasadena, CA 91125, USA*
[18]*Infrared Processing and Analysis Center, California Institute of Technology, Pasadena, CA 91125, USA*
[19]*Instituto de Astrofísica de Canarias, Via Láctea, s/n, 38200 La Laguna, Tenerife, Spain*
[20]*Department of Physics, Yale University, New Haven, CT 06511-8499, USA*

Accepted 2010 November 26. Received 2010 November 17; in original form 2010 August 28

ABSTRACT

We present the details and early results from a deep near-infrared survey utilizing the NICMOS instrument on the *Hubble Space Telescope* centred around massive $M_* > 10^{11}$ $M_\odot$ galaxies at $1.7 < z < 2.9$ found within the Great Observatories Origins Deep Survey (GOODS) fields North and South. The GOODS NICMOS Survey (GNS) was designed to obtain deep *F160W* (*H*-band) imaging of 80 of these massive galaxies and other colour-selected objects such as Lyman-break dropouts, BzK objects, distant red galaxies (DRGs), extremely red objects (EROs), *Spitzer*-selected EROs, BX/BM galaxies, as well as flux-selected submillimetre galaxies. We present in this paper details of the observations, our sample selection, as well as a description of the properties of the massive galaxies found within our survey fields. This includes photometric redshifts, rest-frame colours and stellar masses. We furthermore provide an analysis of the selection methods for finding massive galaxies at high redshifts, including colour-selection methods and how galaxy populations selected through these colour methods overlap. We find that a single colour selection method cannot locate all of the massive galaxies,

⋆E-mail: conselice@nottingham.ac.uk

with no one method finding more than 70 per cent. We however find that the combination of these colour methods finds nearly all of the massive galaxies that would have been identified in a photometric redshift sample, with the exception of apparently rare blue massive galaxies. By investigating the rest-frame $(U - B)$ versus M_B diagram for these galaxies, we furthermore show that there exists a bimodality in colour–magnitude space at $z < 2$, driven by stellar mass, such that the most massive galaxies are systematically red up to $z \sim 2.5$, while lower mass galaxies tend to be blue. We also discuss the number densities for galaxies with stellar masses $M_* > 10^{11}\,\mathrm{M}_\odot$, whereby we find an increase of a factor of 8 between $z = 3$ and 1.5, demonstrating that this is an epoch when massive galaxies establish most of their stellar mass. We also provide an overview of the evolutionary properties of these galaxies, such as their merger histories, and size evolution.

Key words: galaxies: evolution – galaxies: formation – galaxies: structure.

1 INTRODUCTION

Our understanding of distant galaxies and the history of galaxy formation has undergone a revolution in the past decade. Galaxies are now routinely discovered and studied out to redshifts $z \sim$ 4–6 (e.g. Dickinson et al. 2004; Yan et al. 2005; Bouwens et al. 2007; Bouwens et al. 2010). Samples of a few dozen objects have been found at even higher redshift, back to the era of reionization ($z \sim$ 6–7), and perhaps some galaxies have been discovered at even higher redshifts, $z \sim$ 8–10 (e.g. Bouwens et al. 2010; Finkelstein et al. 2010). This relatively rapid advance in our discovery of the earliest galaxies is the direct result of technical advances in spectroscopy and imaging over the past decade, in which the *Hubble Space Telescope* (*HST*) has played a leading role.

Historically, distant galaxies are found within deep optical and near-infrared (NIR) imaging surveys and are confirmed as high-redshift galaxies with large multiobject spectrographs on 8–10 m telescopes, which came online in the mid-1990s. It can be argued however that some of the most important advances in our understanding of galaxies have come about from very deep imaging, especially from *HST*. The *HST* has played a key role in high-redshift discoveries and our understanding of galaxy evolution through large blank field and targeted programmes such as the *Hubble Deep Field* and *Hubble Ultra Deep Field*, Great Observatories Origins Deep Survey (GOODS), EGS and COSMOS among others (e.g. Williams et al. 1996; Giavalisco et al. 2004; Beckwith et al. 2006; Davis et al. 2007; Scoville et al. 2007).

This *Hubble* imaging has proven invaluable for two primary reasons. One is simply due to the depth that can be achieved with a high photometric fidelity, ensuring that exquisite photometry of distant galaxies can be obtained. Whilst ground-based telescopes can reach the depths of *HST* at optical wavelengths, in principle the accuracy and precision of this photometry are not nearly as good due to a higher background and, importantly, the large and variable point spread function (PSF). This makes accurate measurements of light difficult, particularly for colours which require exact apertures for accurate measures. Furthermore, *HST* data have proven important for the discovery of the most distant galaxies in the Universe through the use of the Lyman-break method of looking for drop-out galaxies in bluer bands. Many filter choices within multicolour deep imaging programmes were in fact selected to facilitate optimal drop-out searches (e.g. Giavalisco et al. 2004).

Hubble imaging furthermore has facilitated a renaissance in the study of galaxy structure in the distant Universe, which provides a key observable for understanding how distant galaxies form and evolve (e.g. Conselice et al. 2003; Buitrago et al. 2008; Conselice et al. 2008a,b; Lotz et al. 2008; Bluck et al. 2009; Conselice, Yang & Bluck 2009; Jogee et al. 2009; Cassata et al. 2010). These structural measurements have proven critical for determining how galaxy morphologies, sizes and merger/kinetic states have evolved through time (e.g. Conselice et al. 2003; Ravindranath et al. 2006; Trujillo et al. 2007). This allows us to examine how the role of mergers in galaxy formation has changed (e.g. Conselice et al. 2003, 2008b; Lotz et al. 2008; Jogee et al. 2009), and thus we can begin to derive how galaxies form, as opposed to simply when. It is not currently straightforward to measure the structures of many distant galaxies with ground-based imaging, and thus *Hubble* has and continues to provide a key aspect for tracing evolution using these methods.

However, one key aspect of parameter space that has not yet been explored with *HST*, or other space-based telescopes in any depth over large areas, is deep IR imaging. Previously there exists deep NIC3 imaging over the *Hubble Deep Field* (HDF; Dickinson et al. 2000) and *Hubble Ultra Deep Field* (Thompson et al. 2005), as well as very deep NICMOS imaging over a small area of the HDF-North (HDF-N; Thompson et al. 1999). These areas are however very small, and while NIC3 parallel data exists over the COSMOS and EGS fields, it is quite shallow at ∼1 orbit depth. *HST* imaging data however has a distinct advantage over ground-based imaging not only in terms of the higher quality photometric fidelity and higher resolution, but also in terms of the depth which can be achieved in the NIR with *HST* – as opposed to the ground-based optical where comparable depths to *HST* can be reached. Within one or two orbits, the *HST* can reach a depth in the NIR which is difficult to obtain from the ground even with a 8–10 m class telescope and which will have neither the same photometric quality nor resolution as the *Hubble* data.

We thus designed and carried out the GOODS NICMOS Survey (GNS), which is a large *HST* programme intended to remedy this situation by providing through an initial 180-orbit programme of NIC3 imaging in the GOODS fields, a data set designed to examine a host of problems requiring very deep NIR data. The GNS data consist of 60 NICMOS NIC3 pointings centred on the most massive ($M_* > 10^{11}\,\mathrm{M}_\odot$) galaxies at $1.7 < z < 2.9$. The depth of each image is three orbits/pointing within the H_{160} bandpass over a total area of ∼43 arcmin^2 (Buitrago et al. 2008, Bluck et al. 2009; Bouwens et al. 2009, 2010 and Casey et al. 2009 present results using this data).

With these NICMOS data, we are able to explore the rest-frame optical features of galaxies at $z > 1$ in detail. This allows a few measurements to be made that cannot be easily reproduced with optical imagining and/or deep NIR imaging from the ground. This includes filling in the important NIR gap in galaxy spectral energy distributions (SEDs), sampling the rest-frame optical structures and sizes of galaxies out to $z \sim 3$ (Buitrago et al. 2008) and the detection and characterization of the population of massive $z \sim 7$–10 galaxies and AGN, and determining the relation of AGN evolution to that of massive galaxies (e.g. Bluck et al. 2011).

In this paper, we present the basic outline, background and results from this survey. We discuss the design of the observations, our field selection, as well as the selection for our initial massive galaxy sample which has guided the centres for our NICMOS NIC3 pointings. We also discuss the various methods for locating the massive galaxy population at higher redshifts and the connection of these massive galaxies to those at $z < 2$. We show that no one colour method is able to identify the massive galaxy population at high redshifts and that a combination of methods and photometric redshifts are needed to construct a semicomplete massive galaxy sample at higher redshifts. In this paper, we construct as complete as possible sample of massive galaxies within our fields and discuss the properties of these galaxies, as well as some features of lower mass galaxies.

This paper is organized as follows. Section 2 gives a summary of our observations and the design of the GNS, including how the initial sample of galaxies was selected. Section 3 gives a description of the derived parameters from the H_{160}-band imaging, including photometric redshifts and catalogue matching. Section 4 describes our initial analysis of the survey data, including how the various selections for massive galaxies at high redshifts compare, while finally Section 5 is our summary. We use a standard cosmology of $H_0 = 70\,\mathrm{km\,s^{-1}\,Mpc^{-1}}$ and $\Omega_\mathrm{m} = 1 - \Omega_\Lambda = 0.3$ throughout.

2 OBSERVATIONS

2.1 Survey design

The GNS selection and field coverage is based on the previous optical ACS and ground-based imaging from the original GOODS programme (Giavalisco et al. 2004). The GOODS programme is a multiwavelength campaign to obtain a coherent collection of deep imaging and spectroscopy in two 150-arcmin^2 areas in the Northern and Southern hemispheres (GOODS-N and GOODS-S). These two fields are centred around the HDF-N and *Chandra Deep Field*-South (CDF-S), which are areas of very low dust extinction and minimal stellar and radio contamination. The existing GOODS/ACS fields match the coverage of the GOODS *Spitzer* programme and cover the 2–4 Ms exposure of the CDF-S and the 2-Ms exposure of the CDF-North (CDF-N; Luo et al. 2008). Large ongoing campaigns to obtain spectroscopy for the GOODS fields have also been carried out, including 3000 spectra as part of the Keck Treasury Redshift Survey (Wirth et al. 2004). Another ∼3000 redshifts in GOODS-S have been measured from various European Southern Observatory (ESO) programmes (e.g. Le Fevre et al. 2005; Vanzella et al. 2008; Popesso et al. 2009; Balestra et al. 2010).

The comoving volume probed by GOODS at high redshifts, $2 < z < 6$, is similar to the comoving volume covered by the COSMOS field (e.g. Scoville et al. 2007) at $0.2 < z < 1$. Furthermore, due to its depth at all wavelengths, the GOODS fields are thus an ideal location for examining the formation and evolution of early galaxies. Deep NIR imaging of these fields however is lacking although some deep NIR imaging has been obtained with ESO telescopes using SOFI and ISAAC for the GOODS-S, as well as deep Canada–France–Hawaii Telescope (CFHT) WIRCAM imaging, Subaru imaging and some Keck imaging over the GOODS-N (e.g. Kajisawa et al. 2009; Retzlaff et al. 2010; Wang et al. 2010). However, these data only reach modest depths of $K_\mathrm{vega} \sim 22$ compared to our *HST* imaging. The depth of our survey is only comparable to previous NICMOS deep programmes covering the HDF-N and HDF-South (HDF-S) fields, as well as new NIR data obtained with WFC3 (Cassata et al. 2010).

Ideally, one would want to cover both GOODS fields completely, yet given the small NICMOS field of view it is not practical to cover the entire GOODS fields any deeper than one orbit with NICMOS. The WFC3 camera will, however, soon cover these fields to an even greater depth with the CANDELS program. Our strategy is not to map out a continuous area but to collect 60 pointed observations directed towards the most massive galaxies at $z \sim 1.7$–2.9 found in the GOODS fields (Section 2.2), maximized to obtain the largest number of galaxies based on our selection methods. To obtain the most unique and useful science, we therefore constructed a program which covers a sixth of the area of a single GOODS field (in total 43.7 arcmin^2) in three orbit depths in the H_{160} band, in areas of the deepest *Spitzer*, *Chandra* and ACS imaging, and where the greatest amount of spectroscopy already exists. Some of these fields were then observed in the J band (J_{110}) with NICMOS or WFC3 as part of a follow-up programme to obtain NIR SEDs to look for high-redshift drop-out galaxies (Bouwens et al. 2010).

2.2 Initial galaxy selection

Our NICMOS pointings were chosen to target a set of objects selected as known massive galaxies at high redshift, identified using a variety of colour-selection methods. These include 'distant red galaxies' (DRGs; Franx et al. 2003; Papovich et al. 2006), IRAC extremely red objects (EROs; Yan et al. 2004) and BzK colour-selected galaxies (Daddi et al. 2004, 2007). All of these methods are designed to find red, dusty or passively evolving older galaxies at $z > 1.5$. In practice, we utilized all three of these colour selections separately in order to obtain as much as possible a complete sample of massive galaxies at $z > 2$. To optimize our field placement, we also used catalogues of Lyman-break-selected BM/BX objects (Reddy et al. 2008), as well as high-redshift drop-out and submillimetre galaxies. However, the primary field selection was done in terms of the massive galaxy selection through the three primary colour criteria as described further below.

Colour selection of distant galaxies has a long history dating back to the early work of finding Lyman-break galaxies through image dropouts in blue bands (e.g. Guhathakurta, Tyson & Majewski 1990; Steidel & Hamilton 1992). It is generally accepted that no single method can find all galaxies at a given redshift, and some of these methods are better at finding star-forming objects as opposed to those which are more passive and evolved. In fact, it is generally agreed that no method or combination of methods can identify an obviously complete sample of high-z galaxies to a given depth or stellar mass limit.

One of the methods we use for finding likely passively evolving and dusty red galaxies is to locate DRGs defined by a NIR colour cut (e.g. Franx et al. 2003; Papovich et al. 2006; Conselice et al. 2007b). The selection we use to find DRGs, and to be included within our sample, is galaxies at $z \sim 1.7$–2.9 with $(J - K_\mathrm{s}) > 2.3$ mag in Vega magnitudes (or >1.37 in AB mag) with data down

to a depth of $K_{AB} = 24$ (10σ). The selection for these galaxies is based on ground-based imaging from ISAAC on the Very Large Telescope (VLT). This selection is only used for choosing systems in GOODS-S, as deep NIR imaging over the entire GOODS-N field was not available when the target selection was carried out. This GOODS-S DRG sample is approximately complete for $M_* > 10^{11}\,M_\odot$ DRG-selected galaxies at $z < 3$ (Papovich et al. 2006).

Another selection we use to construct our initial massive sample is the *Spitzer*-selected EROs, otherwise known as IR EROs (IEROs). These were first described in Yan et al. (2004) based on NIR and *Spitzer* data within the GOODS fields. The selection for these objects is $S_\nu(3.6\,\mu m)/S_\nu(0.9\,\mu m) > 20$. These objects were found by Yan et al. (2004), based on SED fits, to have a mixture of old and younger populations. Note that selecting galaxies in this way ensures that they are massive given their brightness in the IR. However, because they are selected with *Spitzer* imaging, which has a large PSF, resulting in potential confusion from neighbouring objects, this selection can have issues with contamination from other galaxies. Hence any galaxies which would satisfy the criteria but are too close to another galaxy will not be included simply due to the problem of confusion.

Another method we use to select distant galaxies is through the BzK approach, which is described in Daddi et al. (2007) in terms of selection within the GOODS fields. The selection for these objects is slightly more complicated than that of the DRGs or IEROs, since they are selected through colours using the B, z and K bands together. This method proposes to separate evolved galaxies or passive pBzKs and those which are star forming or sBzKs. The selection for these galaxies is done through the quantity BzK defined using these three bands by

$$BzK = (z - K)_{AB} - (B - z)_{AB}. \quad (1)$$

Star-forming galaxies at $z > 1.4$ are proposed to have $BzK > -0.2$. The redder, possibly more evolved galaxies, are found through the selection $BzK < -0.2$ and $(z - K)_{AB} > 2.5$. For the BzK sample we use, the selection is somewhat more limited than for the other colour selections as these sources were selected down to $K = 20.5$ Vega in the North and $K = 22$ in the South. We utilize photometric redshifts and stellar masses of the galaxies selected through these methods to identify and study these colour-selected populations taken directly from Papovich et al. (2006), Yan et al. (2004) and Daddi et al. (2007).

Our initial massive galaxy sample from which we optimize our NICMOS pointings are selected through these three methods, with a further photometric redshift cut of $1.7 < z < 2.9$, and with a stellar mass cut of $M_* > 10^{11}\,M_\odot$. In practice our final pointings were chosen by finding the locations within the GOODS fields where the number of these massive galaxies was maximized within the NIC3 fields. In total we imaged 45 pre-selected massive $M_* > 10^{11}\,M_\odot$ galaxies at $1.7 < z < 2.9$ in the GOODS-N and 35 in the GOODS-S.

Galaxies selected in other ways were also used to optimize the number of galaxies in each NIC3 pointing although each pointing was designed to have at least one massive galaxy with the properties above. These 'additional' galaxies are selected through the Lyman-break drop-out method utilizing B, V and i dropouts, the BX/BM selection as well as submillimetre galaxies from Greve et al. (2008). Each NIC3 pointing contained between four and 19 of each of these galaxy types. Fig. 1 shows our field layout within the GOODS fields with the different galaxy types shown as different colours and symbols, and Fig. 2 shows a typical NICMOS NIC3 pointing of one of our fields.

Tables 1 and 2 list the statistics and positions of our 60 pointings, with 30 NIC3 pointings in the GOODS-N field and 30 in GOODS-S. We also list the number of various other types of galaxies within each of these fields. Tables 3 and 4 list the initial massive galaxies for which we picked our fields, along with basic information such as their photometric redshifts, stellar masses and information on the optical and H_{160}-band magnitudes for these systems. NICMOS and ACS images of 10 of these massive galaxies are shown in Fig. 3. This data, including catalogues of sources, redshifts and stellar masses, as well as the original reduced NIC3 imaging itself is available at http://www.nottingham.ac.uk/astronomy/gns/.

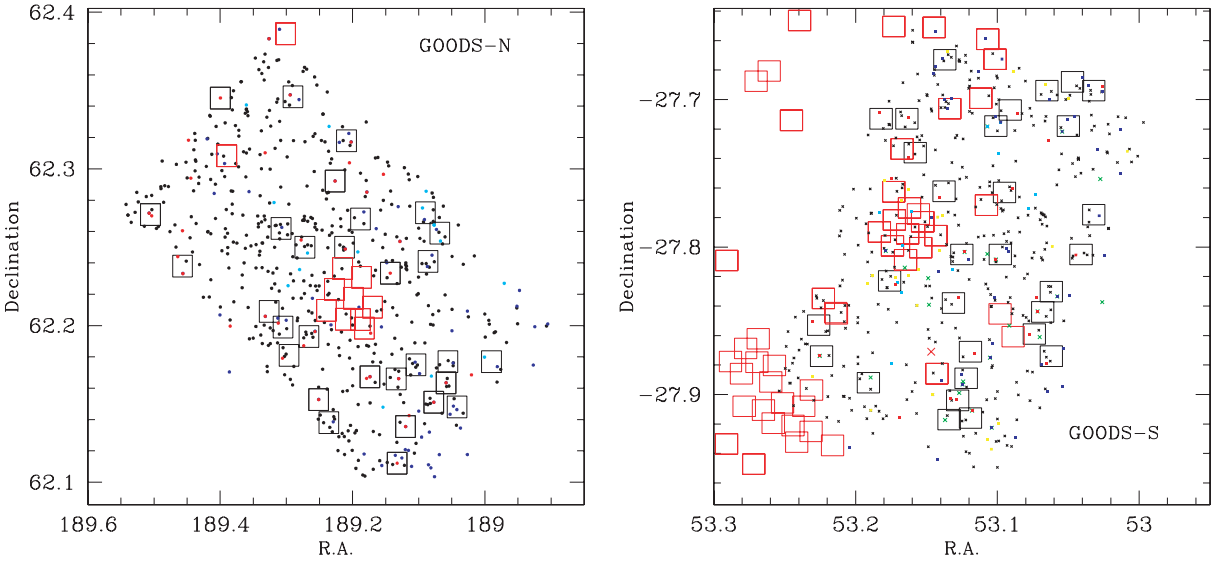

Figure 1. The distribution of the global targets used within the GOODS-N and GOODS-S fields. The points displayed are DRGs (green), IEROs (blue), BzKs (red), IRS *Spitzer* targets (cyan), V-dropouts (black) and high-z galaxies with *Spitzer* IRS spectra (yellow). The black boxes show the locations of the GNS NICMOS pointings, while the red boxes are for previous deep NIC3 fields in these areas. The HDF (within GOODS-N) and the *Hubble Ultra Deep Field* (within GOODS-S) are shown in the centres of each field with overlapping red tiles. Note that these boxes have not been rotated to match the orientation of these fields.

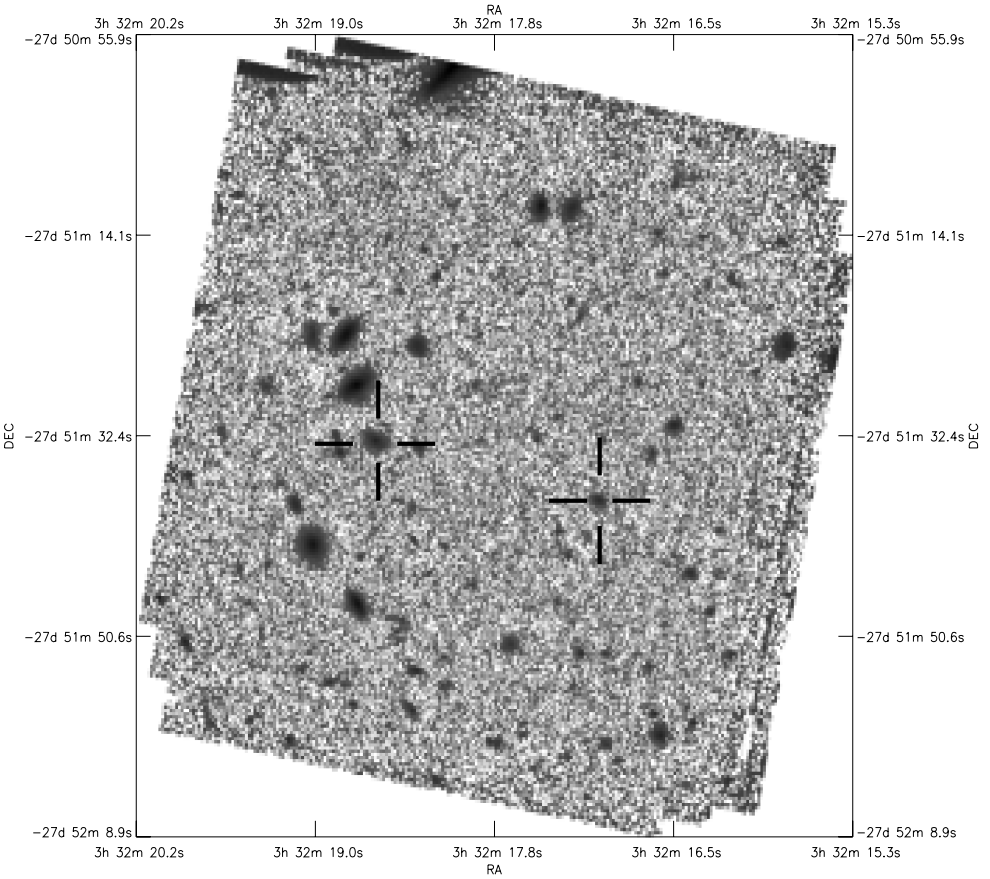

Figure 2. Example of one of our NICMOS images in the H_{160} band. This example is for GOODS-S 16. The field of view of this and all the NICMOS pointings are approximately 51 arcsec on a side. All fields, like this one where positioned to maximize the number of objects observed with NICMOS. We label in this picture the two primary massive galaxies at $z > 2$ within this field.

2.3 Observational parameters and data reduction

For our observations, we used the NIC3 camera in the *H*(*F160W*) (H_{160}) band, with a depth of three orbits per pointing. With this exposure time, we predicted that we would reach $H_{160} = 26.5$ (AB mag) at 5σ for an extended source within a 0.7-arcsec diameter. This imaging, combined with ground-based data at a similar depth, is optimal for measuring photometric redshifts at $z \sim 2$, where the Balmer break occurs for galaxies at these redshifts, and for finding z-band dropouts ($z > 6$) as candidate high-z galaxies (Bouwens et al. 2010).

Our data were processed with the NICMOS reduction package NICRED.PY v1.0. A detailed description of this package can be found in Magee, Bouwens & Illingworth (2007). NICRED v1.0 handles all pipeline-processing steps currently recommended by STScI for NICMOS data. Basic calibration, including zero-read correction, bad pixel masking, noise calculation, dark current subtraction, linearity correction, flat-field correction, photometric calibration and cosmic ray identification, was handled with the IRAF task CALNICA. Pedestal removal and bias subtraction was performed with the IRAF task PEDSKY.

The NICMOS data were taken with three dithers per orbit using a point spacing of 5.06, for a total of nine dithers, which was then used to drizzle the data into the final product. Exposure times are roughly 8100 s per target in the *F160W* band. Each exposure was cleaned of any South Atlantic Anomaly signatures using the algorithm of Bergeron & Dickinson (2003), as implemented in the STScI-PYTHON task saaclean.py. Correction for the 'Mr. Staypuft' anomaly, electronic ghosts due to bright stars in other NICMOS quadrants, was also made using a PYTHON task equivalent to STScI-PYTHON task puftcorr.py.

To improve the overall flatness of individual frames, we median stacked all of the frames associated with the program (after masking out individual sources) to create a supermedian frame. We then subtracted this median from each of the individual exposures. Each exposure was also corrected for the NICMOS count rate non-linearity as identified by Bohlin et al. (2005) and later more thoroughly characterized by de Jong et al. (2006). This latter correction was made using the PYTHON task nonlincor.py.

Because our NICMOS images were taken in a single visit, we did not attempt to correct the relative astrometry of the individual frames to improve the overall alignment solution, although we did adjust the astrometry by 0.3 arcsec in declination when aligning with the GOODS ACS v2.0 imaging. In preparation for the final image combination process, inverse weight maps were computed for each exposure based upon their individual exposure times, the reference darks, and flat fields. Finally, the individual exposures were combined into a final rectified frame with multidrizzle, rejecting any pixel in an exposure that was more than 4σ away from the median defined by the stack. We used a threshold of 3.5σ for the rejection threshold for pixels adjacent to an already rejected pixel.

Table 1. The GOODS-N NICMOS fields with numbers of galaxies of different types.

ID	RA(J2000)	Dec. (J2000)	*V*-drops	*i*-drops	IEROs	BzK	Submillimetre	BX/BM	Other	Total
1	12 36 31.8	62 06 43.7	2	1	4	1	1	0	0	9
2	12 36 28.8	62 08 07.8	1	1	3	1	0	0	0	6
3	12 36 14.1	62 09 48.5	3	0	5	1	0	0	0	9
4	12 36 18.5	62 09 03.7	4	0	2	1	0	0	0	7
5	12 37 00.3	62 09 09.8	0	0	1	1	0	2	0	4
6	12 36 41.7	62 10 02.3	1	0	3	2	0	1	1	8
7	12 36 34.3	62 14 00.4	1	0	0	1	1	2	1	6
8	12 38 01.3	62 16 15.2	1	0	3	2	1	0	0	7
9	12 36 54.3	62 17 31.9	0	0	1	1	0	2	0	4
10	12 37 35.9	62 20 42.9	0	0	2	1	0	0	0	3
11	12 37 11.0	62 10 51.6	3	0	3	1	1	8	0	16
12	12 37 03.8	62 11 34.8	5	2	2	2	0	4	1	16
13	12 36 16.3	62 15 32.4	2	1	3	0	1	5	3	15
14	12 37 05.3	62 15 00.0	5	0	0	1	0	4	2	12
15	12 37 13.2	62 11 56.4	2	0	3	1	1	3	1	11
16	12 37 13.9	62 15 43.2	7	0	1	0	0	3	1	12
17	12 36 13.4	62 10 37.2	4	0	3	0	1	2	0	10
18	12 36 50.9	62 15 00.0	5	1	2	1	0	1	3	13
19	12 36 10.1	62 08 52.8	2	0	7	0	1	0	0	10
20	12 36 21.6	62 16 19.2	2	0	3	0	0	1	1	7
21	12 36 20.6	62 14 27.6	4	0	3	0	0	2	1	10
22	12 36 32.2	62 09 57.6	4	0	4	1	0	1	0	10
23	12 36 56.6	62 08 16.8	5	1	1	0	0	2	0	9
24	12 37 09.6	62 20 45.6	2	0	3	1	1	1	2	10
25	12 36 25.0	62 10 30.0	4	0	5	0	0	0	0	9
26	12 36 45.1	62 16 04.8	2	0	2	0	0	5	0	9
27	12 36 50.2	62 19 04.8	2	0	3	1	1	0	1	8
28	12 37 18.2	62 12 32.4	0	0	1	1	0	5	1	8
29	12 37 49.7	62 14 16.8	1	0	3	2	1	0	0	7
30	12 35 57.6	62 10 39.4	0	1	2	0	0	0	1	4

Note: listed are the centre positions of each NIC3 pointing for the GNS in terms of RA and Dec. Also listed are the number of *V*-drops, *i*-drops, IEROs, BzKs and DRGs. Note that the colour-selected types listed here are not just galaxies with $M_* > 10^{11}$ $M_\odot$, but all galaxies that meet the criteria outlined in Section 2. We also include an 'Other' column which includes the total summation of submillimetre galaxies, galaxies with *Spitzer* IR spectrograph coverage and BM/BX galaxies from Reddy et al. (2008). The total number of galaxies we used to pick these fields is also shown.

We calculated that zero-points for the H_{160} images are 25.17 AB mag and include a correction for the NICMOS non-linearity count rate.[1] In total we obtained 60 pointings for our observations, each one roughly centred on a massive galaxy at $z = 1.7$–2.9. The field of view of each of these images is 51.2 arcsec on a side with a subsampled pixel scale for the final drizzled mosaics of 0.1 arcsec pixel^{-1}. We measure that the FWHM for our images is roughly 0.3 arcsec.

The depth of our data was determined by placing random apertures throughout the images and determining what fraction of simulated sources can be retrieved and by measuring the rms noise at various positions in the imaging. Using this method, we find that the depth at the 5σ limit is 26.8 AB mag using a 0.7-arcsec-diameter aperture. This is similar to our initial estimate based on the expected depth of our imaging.

2.4 SExtractor detections and photometry

After our images were reduced to their three orbit depths we carried out image detection and photometry with the SExtractor package. This is now a standard method for detecting galaxies within imaging, and we only give a brief overview of the methods which we used. The photometry was also done within SExtractor, both for total magnitudes as well as magnitudes measured with a series of apertures.

The basic idea behind SExtractor is to detect objects within an astronomical image and to carry out basic analyses of the photometry and shapes of these objects, typically galaxies and stars. Using SExtractor on an interactive basis, we were able to find an optimal detection and deblending method that accounted for nearly all objects that can be identified as separate galaxies and stars by eye. Weight maps of the exposure times were used within the detection procedure. Overall we find a total of 8298 galaxies within our SExtracting and cleaning process.

We constructed an optically matched catalogue of ACS imaging in the *BViz* bands based on the positions of the galaxies in the NICMOS catalogue. Photometry in *B*, *V*, *i* and *z* bands is available for sources down to a 5σ limiting AB magnitude of $z \sim 27.5$ from the original ACS GOODS survey (Giavalisco et al. 2004) using v2.0 data products. We used the positions of objects in our NICMOS catalogue to match with *BViz* photometry from the ACS v2.0 data. We used AUTOMAG magnitudes to measure the magnitudes for both the *H*-band and the *BViz* magnitudes, which account for the total amount of light within each galaxy at every wavelength. We used these magnitudes to obtain *BVizH* SEDs for every source.

[1] This zero-point differs from that given in the headers of the NICMOS data themselves, because the imaging data are expressed in electrons s^{-1} rather than DN s^{-1}, with a gain of 6.5.

Table 2. The GOODS-S NICMOS fields with numbers of galaxies of different types.

ID	RA (J2000)	Dec. (J2000)	*V*-drops	*i*-drops	IEROs	BzK	DRGs	Other	Total
1	03 32 23.5	−27 48 18.0	3	2	5	1	5	0	16
2	03 32 24.2	−27 43 04.8	2	1	8	0	2	3	16
3	03 32 22.8	−27 45 46.8	3	2	4	1	3	0	13
4	03 32 30.0	−27 48 18.0	2	1	6	1	2	1	13
5	03 32 42.2	−27 49 22.8	4	1	2	1	0	2	10
6	03 32 54.2	−27 51 10.8	2	0	8	1	2	0	13
7	03 32 15.6	−27 41 38.4	3	1	4	0	2	1	11
8	03 32 21.8	−27 42 25.2	1	0	3	1	1	0	6
9	03 32 29.3	−27 53 20.4	2	0	5	0	3	0	10
10	03 32 30.7	−27 54 14.4	1	0	3	2	4	0	10
11	03 32 45.8	−27 53 31.2	2	0	4	0	3	0	9
12	03 32 53.8	−27 52 26.4	2	0	3	1	3	0	9
13	03 32 12.0	−27 43 04.8	1	0	4	0	3	0	8
14	03 32 14.9	−27 52 26.4	3	0	3	1	1	0	8
15	03 32 16.3	−27 50 38.4	3	1	3	1	1	0	9
16	03 32 17.8	−27 51 32.4	1	0	3	1	3	0	8
17	03 32 32.9	−27 40 22.8	3	2	2	0	0	1	8
18	03 32 07.7	−27 41 38.4	3	0	3	1	0	0	7
19	03 32 09.8	−27 48 18.1	4	1	2	1	0	0	8
20	03 32 11.3	−27 41 16.8	2	0	6	0	0	0	8
21	03 32 14.9	−27 49 49.1	3	1	2	0	1	0	7
22	03 32 28.6	−27 54 57.6	2	1	2	1	1	0	7
23	03 32 28.6	−27 52 15.6	1	2	2	1	2	0	8
24	03 32 31.4	−27 50 16.8	2	1	3	1	0	0	7
25	03 32 24.2	−27 55 34.7	3	1	2	0	1	2	9
26	03 32 43.7	−27 42 46.8	3	0	3	1	0	0	7
27	03 32 32.2	−27 55 01.2	1	0	1	2	0	0	4
28	03 32 07.7	−27 46 40.8	2	3	2	0	0	0	7
29	03 32 33.0	−27 45 43.9	2	0	1	1	1	0	5
30	03 32 39.3	−27 42 48.3	4	2	0	1	1	0	8

Note: listed are the centre positions of each NIC3 pointing for the GNS in terms of RA and Dec. Also listed are the number of *V*-drops, *i*-drops, IEROs, BzKs and DRGs. Note that the colour-selected types listed here are not just galaxies with $M_* > 10^{11}$ $M_\odot$, but all galaxies that meet the criteria outlined in Section 2. We also include an 'Other' column which includes the total summation of submillimetre galaxies, galaxies with *Spitzer* IR spectrograph coverage and BM/BX galaxies from Reddy et al. (2008). The total number of galaxies we used to pick these fields is also shown.

These SEDs are used for colour measurements as well as for SED fitting for photometric redshifts and stellar mass calculations. A large fraction of our sources, 1219 out of 8298, have no counterpart in the z band down to the limit of $z_{850} = 27.5$.

After accounting for a well-known 0.3-arcsec offset in the declination direction between the NICMOS and ACS v2.0 data, we find that the average offset between the ACS positions and the NICMOS sources they are identified with is 0.06 ± 0.04 arcsec. We then later use this optical and NIR-matched catalogue to derive properties such as photometric redshifts as well as stellar masses for each of our galaxies. This also allows for us to search for drop-out galaxies which may be at ultrahigh redshift (Bouwens et al. 2010).

We decided to only use *HST* imaging for our photometric catalogue when calculating redshifts and stellar masses to ensure a high fidelity in our photometry. While the GOODS fields have imaging at many ground-based wavelengths (Giavalisco et al. 2004), this imaging is often at a similar wavelength range to an ACS+NICMOS catalogue, with the exception of a few passbands, such as the *U* band and *K* band. The aperture we measure our photometry in is furthermore large enough such that the different PSFs within NICMOS and ACS do not affect our measurements. The accuracy of our matched photometry is very high, and our depth is much greater than any ground-based imaging, and thus to obtain a cleaner measurement we have limited our analysis to these five bands. Furthermore, we do not use *Spitzer* IRAC photometry for our galaxies (although we have matched these) simply because of issues related to contamination and deblending which can be substantial for galaxies which are separated by less than the PSF of the IRAC imaging [several arcsec in full width at half-maximum (FWHM)], making measurements of our photometry and stellar masses much more difficult.

2.4.1 *Number counts*

In Fig. 4, we present the number counts for our H_{160}-band imaging, with a comparison to counts from the HDF-S (Metcalfe et al. 2006) and the HDF-N (Thompson et al. 1999). Based on a comparison to these H_{160} counts, we are roughly complete in our galaxy selection to $H_{160} = 25.5$. The scatter in the counts at the faint end are most certainly due to cosmic variance effects, given the small field of view of these previous surveys. There are, however, some differences, particularly at the faint end of the counts, which can also be seen by comparing the HDF-S and HDF-N counts. This shows that we are obtaining similar photometric quality to these previous deeper NICMOS pointings and our reduction and detection processes are consistent with previous work.

3 DERIVED PARAMETERS

There are two primary catalogues used within the GNS. The first is the initial catalogue of massive galaxies selected by the methods

Table 3. Basic information and photometry for our initial colour-selected sample of galaxies with $M_* > 10^{11}\,M_\odot$ within the GOODS-N field.

ID	Type	RA (J2000)	Dec. (J2000)	z_{phot}	M_* ($\times 10^{11}\,M_\odot$)	B_{450}	V_{606}	i_{775}	z_{850}	H_{160}
43	4	189.125549	62.115509	2.20	1.21	27.05 ± 0.32	26.82 ± 0.20	26.04 ± 0.16	25.44 ± 0.10	22.60 ± 0.10
77	1	189.132522	62.112205	1.91	2.57	27.82 ± 0.86	26.89 ± 0.27	25.76 ± 0.14	25.01 ± 0.08	22.07 ± 0.06
21	4	189.135406	62.117168	2.70	1.11	26.16 ± 0.07	25.60 ± 0.03	25.35 ± 0.03	25.34 ± 0.04	23.96 ± 0.16
227	5	189.119278	62.135971	2.07	1.59	26.60 ± 0.13	26.48 ± 0.10	26.58 ± 0.17	26.32 ± 0.15	25.23 ± 0.26
373	5	189.058517	62.163517	2.50	1.16	–	–	–	–	22.80 ± 0.07
552	5	189.077056	62.151042	1.92	2.12	24.92 ± 0.09	24.44 ± 0.06	23.61 ± 0.04	23.10 ± 0.03	21.08 ± 0.03
730	5	189.251312	62.152904	2.47	1.23	–	–	–	–	24.35 ± 0.15
840	5	189.173446	62.167392	1.92	2.01	27.30 ± 0.33	26.30 ± 0.11	25.65 ± 0.0908	25.02 ± 0.06	22.15 ± 0.06
856	1	189.178649	62.166355	1.74	2.41	28.24 ± 0.96	26.87 ± 0.23	25.66 ± 0.1146	24.83 ± 0.06	21.77 ± 0.05
999	1	189.142868	62.233570	1.98	1.47	26.23 ± 0.17	25.17 ± 0.07	24.27 ± 0.0463	23.38 ± 0.02	21.56 ± 0.06
1144	5	189.503555	62.270061	2.07	1.34	28.80 ± 0.65	28.69 ± 0.47	–	26.99 ± 0.18	22.29 ± 0.08
1129	5	189.507492	62.271797	2.37	1.54	29.34 ± 0.77	28.28 ± 0.23	27.60 ± 0.20	27.65 ± 0.23	23.21 ± 0.13
1257	5	189.226257	62.292339	2.02	1.00	29.64 ± 2.00	29.03 ± 1.03	26.57 ± 0.17	26.27 ± 0.14	23.13 ± 0.09
1394	5	189.399597	62.345371	2.04	2.27	27.56 ± 0.43	27.57 ± 0.37	26.90 ± 0.33	25.71 ± 0.12	22.26 ± 0.06
1533	1	189.305038	62.179489	2.56	1.33	25.86 ± 0.12	25.57 ± 0.08	25.13 ± 0.08	25.10 ± 0.09	24.38 ± 0.19
1666	5	189.256576	62.196266	2.36	2.38	27.61 ± 0.58	26.90 ± 0.27	25.77 ± 0.14	25.30 ± 0.10	21.50 ± 0.05
1768	1	189.273559	62.187240	1.95	2.08	28.39 ± 0.95	27.31 ± 0.28	26.68 ± 0.25	25.53 ± 0.09	22.20 ± 0.12
1826	4	189.073135	62.261402	2.20	1.89	25.34 ± 0.06	25.21 ± 0.05	25.09 ± 0.07	24.64 ± 0.05	22.60 ± 0.06
1942	1	189.277557	62.254707	2.51	1.07	25.07 ± 0.05	24.61 ± 0.03	24.35 ± 0.04	24.07 ± 0.03	22.15 ± 0.05
2066	4	189.300201	62.203414	2.80	2.24	26.54 ± 0.19	26.83 ± 0.19	25.79 ± 0.12	25.66 ± 0.12	23.21 ± 0.13
2083	1	189.312072	62.201652	2.72	1.91	27.77 ± 0.45	27.65 ± 0.30	26.79 ± 0.22	25.99 ± 0.11	22.83 ± 0.09
2049	4	189.312988	62.204704	2.40	1.62	–	–	–	–	23.28 ± 0.22
2282	4	189.306976	62.262676	2.30	1.34	28.70 ± 0.71	28.12 ± 0.34	27.95 ± 0.41	26.98 ± 0.18	23.57 ± 0.11
2411	4	189.047927	62.176132	2.10	1.48	27.61 ± 0.44	26.44 ± 0.13	26.05 ± 0.15	25.54 ± 0.10	22.68 ± 0.09
2564	5	189.210907	62.248912	1.83	1.36	–	27.64 ± 0.40	26.46 ± 0.22	25.13 ± 0.07	22.26 ± 0.07
2734	4	189.042160	62.146274	2.60	1.06	30.15 ± 1.85	28.02 ± 0.22	27.76 ± 0.31	27.25 ± 0.21	23.83 ± 0.13
2678	4	189.047424	62.148479	2.50	3.41	–	27.23 ± 0.29	26.36 ± 0.23	25.50 ± 0.11	22.18 ± 0.05
2764	4	189.052475	62.143322	2.20	1.42	26.70 ± 0.17	26.21 ± 0.09	25.60 ± 0.09	25.20 ± 0.07	22.97 ± 0.12
2902	4	189.091293	62.267700	2.00	1.67	28.33 ± 0.77	27.16 ± 0.22	26.53 ± 0.20	25.95 ± 0.13	23.17 ± 0.14
2837	4	189.094375	62.275016	2.30	2.45	25.16 ± 0.08	25.02 ± 0.06	24.62 ± 0.07	24.26 ± 0.05	22.68 ± 0.07
2965	4	189.079818	62.244968	2.80	1.34	29.24 ± 2.75	26.26 ± 0.13	25.11 ± 0.07	25.14 ± 0.08	23.06 ± 0.11
3036	4	189.087020	62.237724	2.10	1.28	25.37 ± 0.10	24.93 ± 0.06	24.63 ± 0.06	24.01 ± 0.04	22.34 ± 0.07
3126	5	189.130340	62.166198	2.10	1.23	27.50 ± 0.44	26.44 ± 0.13	26.00 ± 0.15	25.29 ± 0.09	23.18 ± 0.10
3250	4	189.229095	62.138568	2.30	1.32	26.34 ± 0.12	26.44 ± 0.09	26.01 ± 0.10	26.04 ± 0.11	23.11 ± 0.11
3422	4	189.280883	62.344234	2.80	1.24	28.26 ± 0.51	26.82 ± 0.14	26.69 ± 0.17	26.47 ± 0.15	23.79 ± 0.19
3387	5	189.294021	62.347286	1.84	1.02	28.65 ± 1.15	27.52 ± 0.29	26.53 ± 0.16	25.75 ± 0.09	22.73 ± 0.08
3582	4	189.098754	62.169300	2.40	1.51	–	–	–	–	23.68 ± 0.20
3629	4	189.182952	62.272567	2.10	1.91	26.56 ± 0.19	25.44 ± 0.05	24.88 ± 0.05	24.40 ± 0.04	21.82 ± 0.06
3818	5	189.202041	62.317256	1.75	2.59	28.26 ± 1.36	26.47 ± 0.25	25.28 ± 0.13	24.15 ± 0.05	21.52 ± 0.05
3766	4	189.205612	62.322628	2.10	1.56	26.10 ± 2.00	25.44 ± 0.08	24.86 ± 0.08	24.51 ± 0.06	22.14 ± 0.06
3822	4	189.219863	62.316909	2.20	1.16	–	29.61 ± 1.19	28.48 ± 0.62	27.36 ± 0.24	23.46 ± 0.09
3970	5	189.331710	62.205925	2.34	1.44	27.66 ± 0.43	27.02 ± 0.18	26.15 ± 0.13	25.87 ± 0.11	23.00 ± 0.10
4121	5	189.456344	62.233276	1.92	1.59	–	26.29 ± 0.08	25.11 ± 0.04	24.70 ± 0.03	21.92 ± 0.08
4033	1	189.464111	62.244133	2.07	1.10	24.82 ± 0.07	24.54 ± 0.06	23.86 ± 0.05	23.68 ± 0.05	21.61 ± 0.04
4239	4	188.981262	62.173790	2.20	1.50	26.47 ± 0.22	25.97 ± 0.11	25.70 ± 0.14	25.05 ± 0.09	22.99 ± 0.13

Note: the ID for each object is from our final NIC3 catalogue of objects, the column 'Type' refers to the colour-selection method in which these galaxies were found, with 1 = BzK, 4 = IERO, 5 = BzK+IERO; z_{phot} is the initial measured photometric redshift, whose accuracy is described in Section 3.2, and which depends upon both redshift and magnitude; M_* is the stellar mass in units of $10^{11}\,M_\odot$ with an average uncertainty of ± 0.25 dex. The remaining panels give our *BVizH* photometry for these systems.

described in Section 2.2. The other is the SExtractor-based catalogue of the survey based on the H_{160}-band imaging. This catalogue is an H_{160}-band catalogue of every object which is imaged within the NIC3 survey, regardless of mass and brightness. These two catalogues will be used for different purposes throughout this study, and in the follow-up papers, with detailed analyses of various aspects of this work. We describe in this section the redshift and stellar mass data we use to construct the first sample from which our initial targets were chosen. We also describe in detail the redshifts and stellar masses derived from the new optical+NIR catalogue, which we constructed using our H_{160}-band-selected objects matched to the optical ACS photometry.

3.1 Photometric redshift measurements

To obtain photometric redshifts, the NICMOS H_{160}-band sources are matched to the catalogue of optical sources in the GOODS-ACS fields as described in Section 2.4. Photometric redshifts are then obtained by fitting template spectra to the *BVIzH* photometric data points. We do not include other wavebands or ground-based data; we omit these so that we can obtain the highest fidelity photometry not affected by zero-point random and systematic errors, background noise or confusion with other sources as described in Section 2.3. The degeneracy in colour-redshift space is problematic, especially when few filters are available. To cope with this effect, we used two different approaches: the standard χ^2 minimization procedure,

Table 4. Basic information and photometry for our initial colour selected sample of galaxies with $M_* > 10^{11}$ M$_\odot$ within the GOODS-S field.

ID	Type	RA (J2000)	Dec. (J2000)	$z_{\rm phot}$	M_* ($\times 10^{11}$ M$_\odot$)	B_{450}	V_{606}	i_{775}	z_{850}	H_{160}
4299	6	53.0918007	−27.8028107	2.40	2.13	27.01 ± 0.19	25.78 ± 0.06	25.65 ± 0.08	25.47 ± 0.08	25.32 ± 0.22
4281	6	53.0938988	−27.8011951	2.60	1.20	25.63 ± 0.05	25.49 ± 0.04	25.40 ± 0.07	25.21 ± 0.06	24.48 ± 0.14
4348	3	53.1008377	−27.8082333	1.97	1.61	–	29.03 ± 0.62	27.20 ± 0.20	27.24 ± 0.23	25.28 ± 0.28
4434	6	53.0976601	−27.7153015	2.14	1.15	25.80 ± 0.07	25.18 ± 0.04	24.80 ± 0.04	24.49 ± 0.03	22.44 ± 0.05
4399	4	53.1008263	−27.7117653	2.30	1.25	26.96 ± 0.18	26.47 ± 0.10	26.24 ± 0.14	26.20 ± 0.15	24.71 ± 0.23
4557	3	53.0891876	−27.7600765	2.27	1.62	27.40 ± 0.51	26.88 ± 0.29	25.93 ± 0.20	24.82 ± 0.08	21.94 ± 0.08
4754	6	53.1201096	−27.8082657	2.00	3.18	29.09 ± 1.06	28.38 ± 0.51	27.14 ± 0.28	26.30 ± 0.14	22.73 ± 0.08
4706	7	53.1231232	−27.8033943	2.34	1.25	28.06 ± 0.54	26.44 ± 0.09	25.63 ± 0.07	24.99 ± 0.04	22.16 ± 0.08
4882	5	53.1717033	−27.8256683	1.74	1.25	27.61 ± 0.40	26.34 ± 0.11	25.14 ± 0.06	24.36 ± 0.04	21.97 ± 0.05
4941	1	53.2300110	−27.8507748	1.83	1.02	26.87 ± 0.17	26.38 ± 0.10	26.14 ± 0.13	26.34 ± 0.17	21.60 ± 0.05
5171	6	53.0632668	−27.6996498	2.39	1.03	26.39 ± 0.12	25.56 ± 0.05	25.04 ± 0.05	24.84 ± 0.05	22.94 ± 0.08
5281	5	53.0859909	−27.7091026	2.10	1.24	–	28.37 ± 0.35	27.33 ± 0.22	27.31 ± 0.25	25.59 ± 0.26
5445	6	53.1245880	−27.8932495	2.50	2.85	–	–	–	–	23.54 ± 0.12
5372	4	53.1255684	−27.8864536	2.90	1.21	27.35 ± 0.24	26.14 ± 0.08	25.77 ± 0.10	25.69 ± 0.10	23.62 ± 0.15
5533	7	53.1289139	−27.9036846	2.79	1.25	–	–	–	–	23.60 ± 0.11
5524	3	53.1332588	−27.9029388	2.58	1.47	–	26.22 ± 0.06	25.20 ± 0.04	25.09 ± 0.04	22.17 ± 0.07
5764	7	53.2252083	−27.8738060	2.65	1.88	–	28.23 ± 0.46	27.21 ± 0.29	26.50 ± 0.17	22.66 ± 0.07
5853	6	53.0508537	−27.7137222	2.41	2.76	26.35 ± 0.20	25.70 ± 0.09	25.61 ± 0.15	25.05 ± 0.11	23.25 ± 0.15
5933	6	53.0542488	−27.7216587	2.30	1.82	–	28.94 ± 0.47	28.00 ± 0.33	27.54 ± 0.26	23.32 ± 0.11
6035	4	53.0555954	−27.8740025	1.90	2.08	27.52 ± 0.00	26.98 ± 0.23	25.73 ± 0.13	25.21 ± 0.10	21.85 ± 0.06
6114	1	53.0656776	−27.8788643	2.24	1.30	28.19 ± 0.66	26.20 ± 0.10	25.57 ± 0.09	24.50 ± 0.04	21.92 ± 0.05
6220	7	53.0717087	−27.8436356	1.90	1.02	27.19 ± 0.37	26.79 ± 0.19	25.91 ± 0.14	25.27 ± 0.09	22.50 ± 0.07
6352	7	53.0773201	−27.8595829	1.96	1.19	–	28.90 ± 0.62	28.65 ± 0.83	27.00 ± 0.21	22.37 ± 0.08
6468	4	53.1385193	−27.6717854	2.80	2.82	25.92 ± 0.18	26.12 ± 0.16	25.25 ± 0.12	24.78 ± 0.08	22.80 ± 0.10
6584	5	53.0260849	−27.6909122	1.99	1.18	26.54 ± 0.0	27.42 ± 0.56	25.95 ± 0.25	24.50 ± 0.09	22.07 ± 0.09
6575	4	53.0354462	−27.6900806	2.50	2.58	25.03 ± 0.07	26.12 ± 0.16	25.53 ± 0.16	24.61 ± 0.08	22.54 ± 0.12
6876	4	53.0400429	−27.6852055	2.50	2.83	26.30 ± 0.00	27.08 ± 0.27	25.98 ± 0.17	25.55 ± 0.15	22.98 ± 0.16
7090	6	53.0578766	−27.8335018	2.70	4.75	–	–	–	–	22.22 ± 0.06
7155	3	53.1175194	−27.9107571	2.69	1.47	28.32 ± 0.73	26.84 ± 0.17	26.09 ± 0.14	26.10 ± 0.16	24.70 ± 0.39
7320	7	53.1156578	−27.8717003	2.07	1.01	–	–	–	–	26.36 ± 0.53
7425	6	53.1271477	−27.8345642	1.81	1.64	27.46 ± 0.36	26.21 ± 0.15	24.91 ± 0.08	23.91 ± 0.03	21.59 ± 0.06
7677	5	53.1830482	−27.7089996	1.76	3.73	26.32 ± 0.26	25.55 ± 0.11	23.80 ± 0.04	22.79 ± 0.02	20.62 ± 0.04
7970	4	53.0282135	−27.7788277	2.30	1.41	27.80 ± 0.52	27.56 ± 0.38	26.22 ± 0.18	25.77 ± 0.14	22.69 ± 0.06
8140	1	53.1410255	−27.7667332	1.91	1.64	25.76 ± 0.10	25.10 ± 0.06	24.45 ± 0.05	23.69 ± 0.03	21.47 ± 0.05
8213	3	53.1628799	−27.7122879	2.14	1.44	23.05 ± 0.02	22.83 ± 0.01	22.30 ± 0.01	22.07 ± 0.01	21.97 ± 0.06

Note: the ID for each object is from our final NIC3 catalogue of objects. The column 'Type' refers to the colour-selection method in which these galaxies were found, with 1 = BzK, 3 = BzK+DRG, 4 = IERO, 5 = BzK+IERO, 6 = DRG+IERO, 7 = BzK+DRG+IERO; $z_{\rm phot}$ is the initial measured photometric redshift, whose accuracy is described in Section 3.2, and which depends upon both redshift and magnitude; M_* is the stellar mass in units of 10^{11} M$_\odot$ with an average uncertainty of ±0.25 dex. The remaining panels give our *BVizH* photometry for these systems.

using HYPERZ (Bolzonella et al. 2000), and a Bayesian approach using the BPZ method (Benitez 2000).

The synthetic spectra used by HYPERZ are constructed with the Bruzual & Charlot (2003, hereafter BC03) evolutionary code, representing roughly the different types of galaxies found in the local Universe. We use five template spectra corresponding to the spectral types of E, Sa, Sc and Im, as well as a single starburst model. The reddening law is taken from Calzetti et al. (2000). The code then computes the most likely redshift solution in the parameter space of age, metallicity and reddening. The best-fitting redshift and corresponding probability are then output together with the best-fitting parameters of spectral type, age, metallicity, A_V and secondary solutions of these.

The Bayesian approach of Benitez (2000) uses a similar template-fitting method, as well as using an empirical rather than synthetic template SEDs. The main difference of this approach from HYPERZ is that it does not rely on the maximum likelihood of the redshift solution in the parameter space as described above. Instead it uses additional empirical information about the likelihood of a certain combination of parameters, also known as prior information or priors. The redshift solution with the maximum likelihood is determined after weighting the probability of each solution by the additional probability determined from the prior information. In our case, the prior is the distribution of magnitudes for different morphological types as a function of redshift obtained from HDF-N data (Benitez 2000). In short, the code not only determines the best-fitting redshift and spectral type, but also takes into account how likely is it to find a galaxy of that spectral type and magnitude at the given redshift.

3.2 Comparison with spectroscopic redshifts

Since the spectroscopic redshifts of sources in the two GOODS fields (North and South) were taken from different compilations of data, we compare them separately to the photometric redshifts from their respective fields in this section.

Spectroscopic redshifts of sources in the GOODS-N field were compiled by Barger et al. (2008), whereas in the GOODS-S field spectroscopic redshifts are taken from the FIREWORKS compilation (Wuyts et al. 2008). The original sources for these redshifts are many, and include papers such as Wirth et al. (2004) and Reddy et al. (2008), and we refer to these compilations for the full list of sources

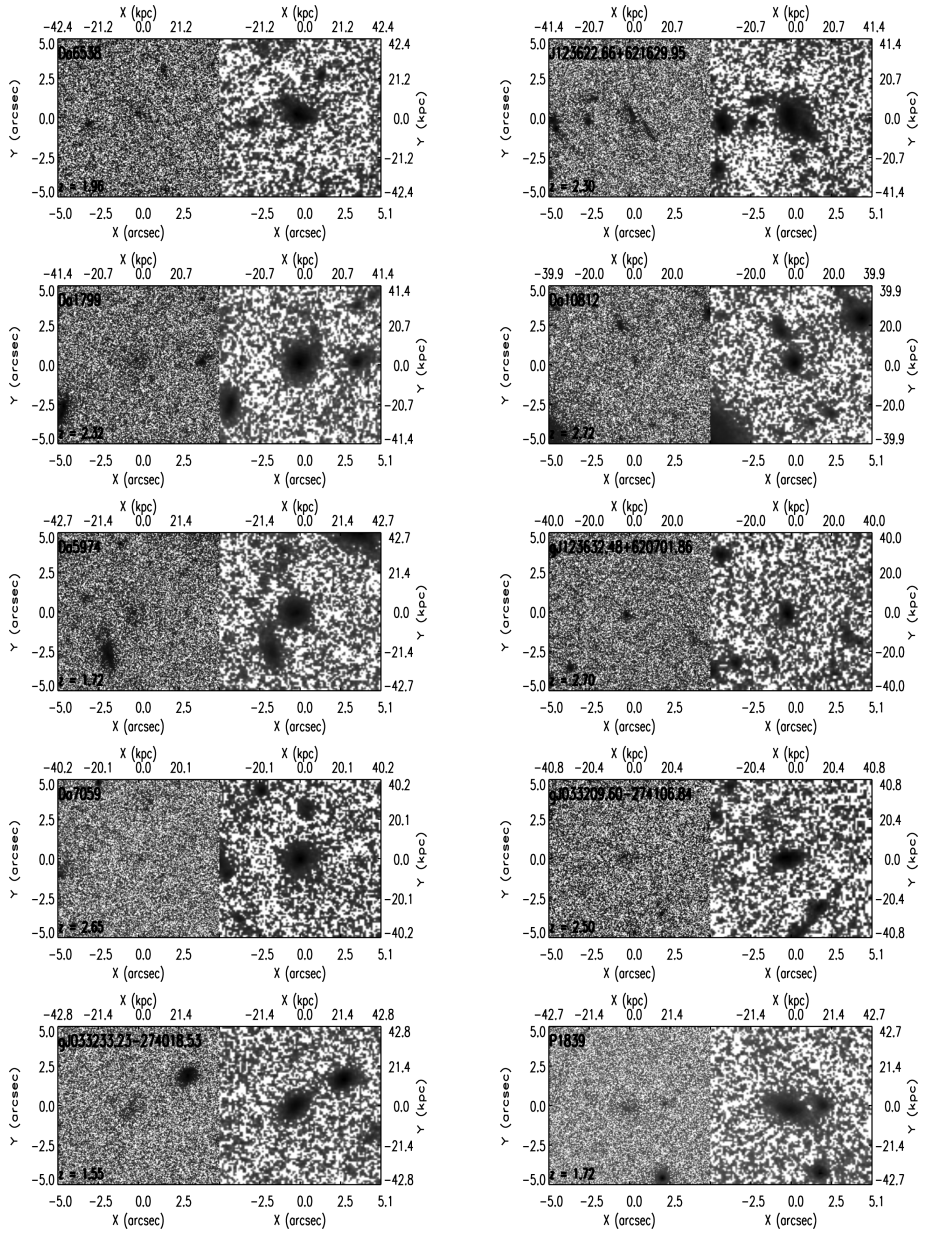

Figure 3. Montage of example GNS massive galaxies with $M_* > 10^{11}\,\mathrm{M}_\odot$. Shown on the left-hand side of each image is the galaxy in the ACS z band, while the right-hand side shows the NICMOS NIC3 H_{160}-band view of the same galaxy. The sizes in kpc are on the top and in arcsec on the bottom.

from which these redshifts were collated. We matched these catalogues to our photometric catalogue, obtaining 537 spectroscopic redshifts for our sources in GOODS-N and 369 in GOODS-S. The mean separation between photometric and spectroscopic sources is 0.41 ± 0.06 arcsec in the GOODS-N field and 0.13 ± 0.05 arcsec in the GOODS-S field.

The reliability of photometric redshift measures is often defined by $\Delta z/(1+z) \equiv (z_{\rm spec} - z_{\rm phot})/(1+z_{\rm spec})$. In the following, we compare the median error ($\langle \Delta z/(1+z) \rangle$) and rms scatter ($\sigma$) as well as the fraction of catastrophic outliers, i.e. galaxies with both $|\Delta z/(1+z)| > 0.5$ and >0.2, obtained by the two methods described above.

We find good agreement between photometric and spectroscopic redshifts for both codes. However, HYPERZ gives slightly better results although BPZ gives higher probability (P) redshifts. Using HYPERZ, we obtain the following results: sources in the GOODS-N field have an $\langle \Delta z/(1+z) \rangle = 0.027$, with a scatter of $\sigma = 0.04$ (222 out of 537 galaxies with $P > 95$ per cent). Sources in the GOODS-S field show similar values: $\langle \Delta z/(1+z) \rangle = 0.043$ and $\sigma = 0.04$ (134 of 369 with $P > 95$ per cent). BPZ gives slightly higher errors and scatter: $\langle \Delta z/(1+z) \rangle = 0.07$ and $\sigma = 0.05$ for GOODS-N (475 galaxies) and $\langle \Delta z/(1+z) \rangle = 0.07$ and $\sigma = 0.06$ for GOODS-S (317 galaxies). We find that galaxies with lower probability redshifts give similar accuracy when compared to spectroscopic redshifts. We therefore use all of the photometric redshifts calculated within our analysis. The fraction of catastrophic outliers is $\sim$6 per cent for both codes. It rises to $\sim$16 per cent for galaxies with $|\Delta z/(1+z)| > 0.2$. Surveys of high-z galaxies using multiple medium band NIR filters find photometric redshifts similar to ours, with $\Delta z/(1+z) \sim 0.2$ (van Dokkum et al. 2009).

The relatively good agreement between photometric and spectroscopic redshifts is shown in Fig. 5. The photometric redshifts

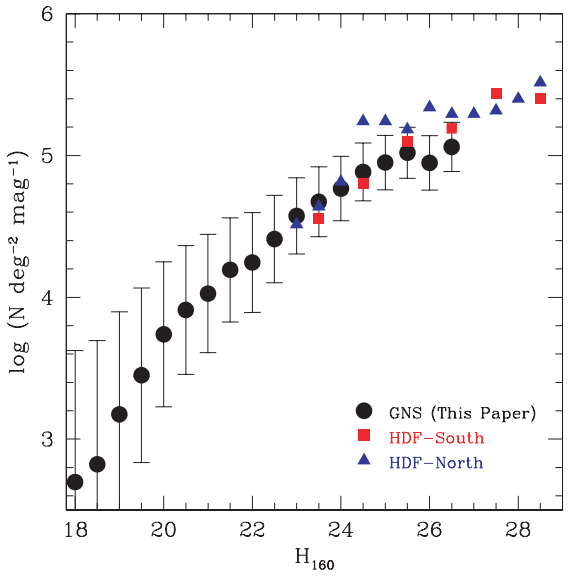

Figure 4. Number counts within our GNS H_{160}-band imaging. Shown for comparison are number counts from the HDF-N and HDF-S imaging which were taken using the same camera and filter. Data for the HDF-S originates from Metcalfe et al. (2006) and the HDF-N number counts are from Thompson et al. (1999).

of the HYPERZ code are plotted against the spectroscopic redshifts in the GOODS-N and GOODS-S. Objects with a high probability value of $z_{\rm phot}$ are encircled in red. Most outliers, especially at low redshift do not have a high probability. The lower panel shows the $\Delta z/(1+z)$ dependence on redshift $z_{\rm spec}$, where there is no clear trend, or bias, with redshift, with the possible exception of a slight trend to underestimate redshifts at high z.

Since most of the galaxies we study in the GNS are at $z > 2$, it is worth discussing briefly the fact that the photometric redshifts decline slightly in quality at these higher redshifts. For the high-redshift sample at $1.5 < z < 3.0$, we find an average photometric redshift offset of $\langle \Delta z/(1+z) \rangle = 0.06$ and a rms of $\sigma = 0.10$. We further find that the fraction of catastrophic outliers within this redshift range is 20 per cent. Catastrophic outliers are defined as galaxies with $|\Delta z/(1+z)| > 0.3$, which corresponds to ∼3 times the rms scatter. Galaxies below $z = 1.5$ show a slightly lower, but still comparable scatter of $\sigma = 0.08$; however the outlier fraction decreases dramatically to only ∼2 per cent.

We are also interested in how good our photometric redshifts are with respect to our selection method for our sample, which uses the H_{160} band. Thus Fig. 6 shows the dependence of $\Delta z/(1+z)$ on H_{160}-band magnitude. HYPERZ and BPZ results are plotted in red and blue, respectively. Only high probability redshifts are used in this figure. The median error and rms scatter computed in each magnitude are shown. The figure shows the slightly better performance of HYPERZ,

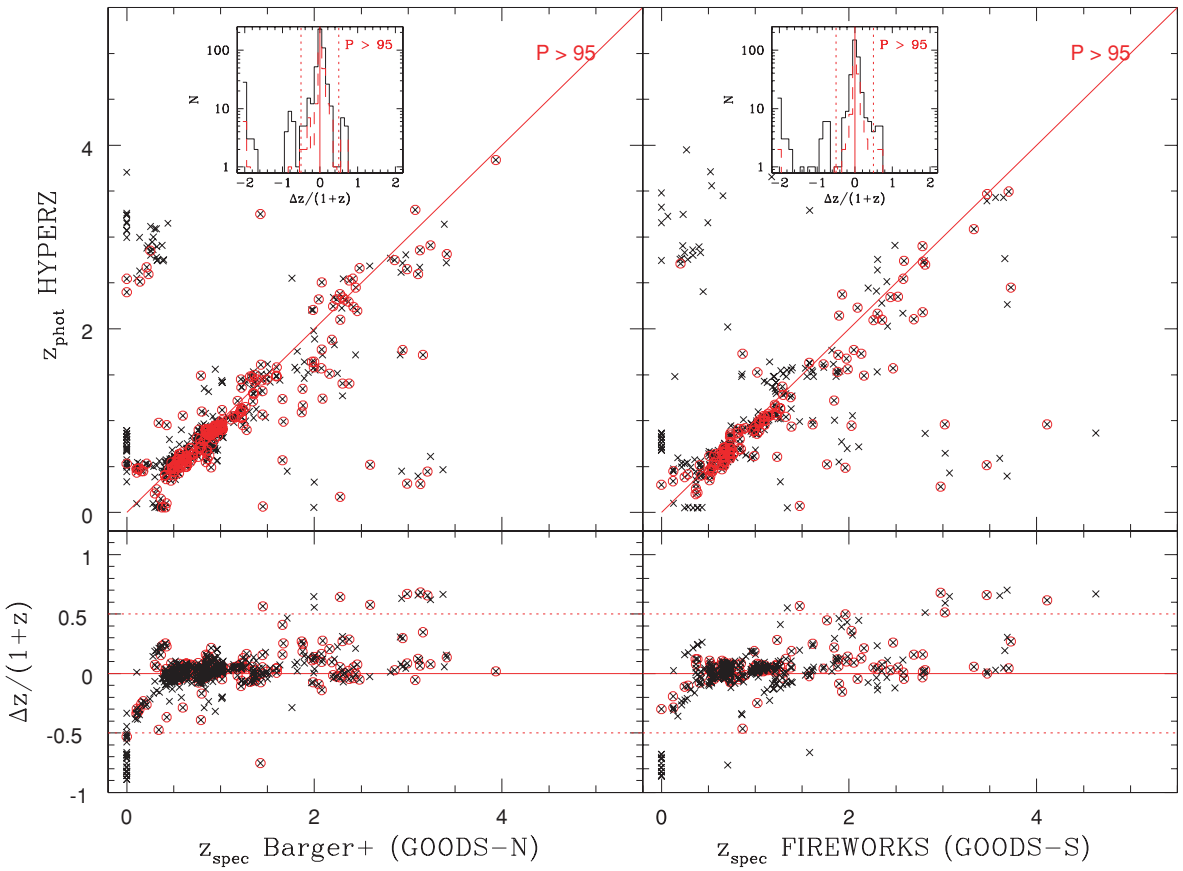

Figure 5. Reliability of photometric redshifts. Top panels: photometric versus spectroscopic redshifts in the GOODS-N (left-hand panel) and GOODS-S (right-hand panel) fields for galaxies with redshift probabilities (P) greater than 95 per cent. The insets show the distribution of $\Delta z/(1+z)$ for all photometric redshifts (black) and high probability redshifts only (red, long dashed). Bottom panels: $\Delta z/(1+z)$ dependence on redshift. Black symbols show all redshifts, red symbols high probability redshifts only. The dashed lines in all the panels and subpanels show a limit for catastrophic outliers at $|\Delta z/(1+z)| > 0.5$.

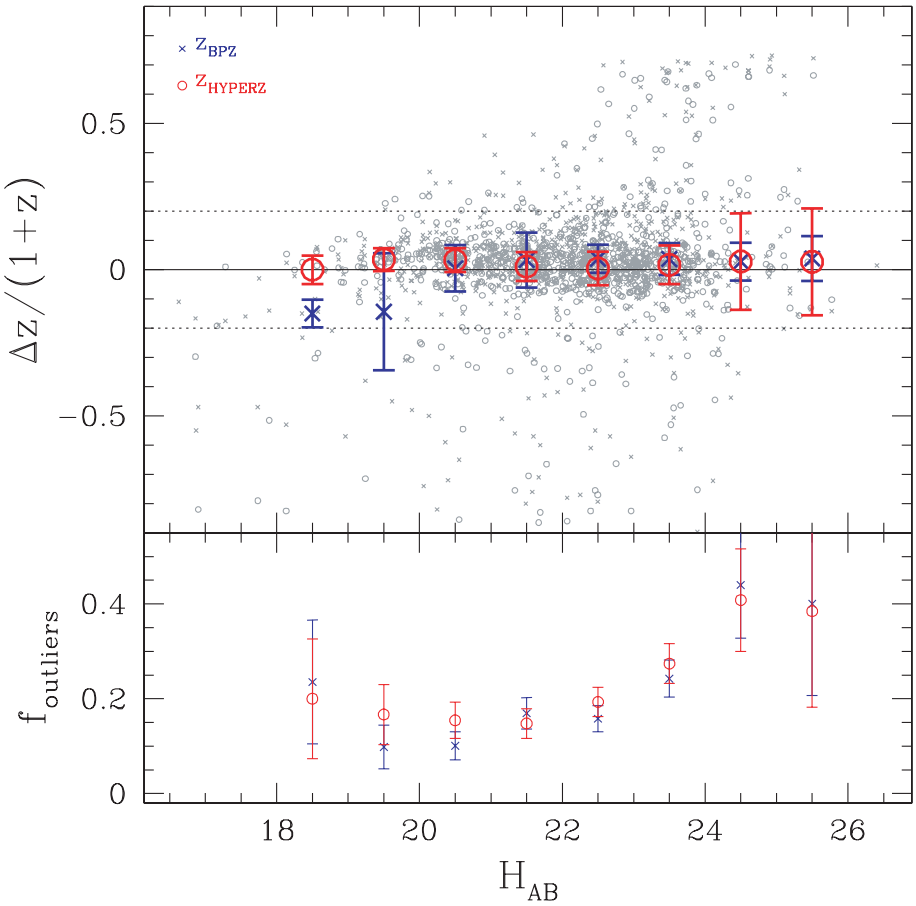

Figure 6. Dependence of $\Delta z/(1+z)$ on H_{160} magnitude. Top panel: $\Delta z/(1+z)$ versus H_{160}-band magnitude for HYPERZ (red circles) and BPZ (blue crosses) results. Median values in each magnitude bin (width = 1 mag) are plotted as solid lines, with the rms scatter shaded in the respective colour. Bottom panel: fraction of catastrophic outliers $|\Delta z/(1+z)| > 0.5$ as a function of H_{160}-band magnitude. Only high probability redshifts are used in this plot.

which is also visible in the fraction of outliers with $|\Delta z/(1+z)| > 0.5$. The redshift error is stable up to faint magnitudes of $H_{160} \sim 24$, as is the fraction of outliers. HYPERZ is likely giving a superior result over BPZ due to the limited redshifts we can use as the Bayesian training set, which thus limits the reliability of redshifts and/or types of galaxies for which no spectroscopic redshifts are available. See also Conselice et al. (2007a) for a more general discussion about using different types of photometric redshifts for galaxies with different properties.

The comparison of our results with photometric redshifts already available for the brighter part of our sample shows that our photometric redshifts are of comparable quality to those using many more photometric bands although these necessarily are from ground-based and/or *Spitzer* imaging. Photometric redshifts taken from the FIREWORKS compilation have a median difference of $\Delta z/(1+z) = 0.037$ and an rms scatter of $\sigma = 0.028$ in comparison to our photometric redshifts. While we find good agreement between our photometric redshifts and previously published spectroscopic redshifts, it must be noted that most of these galaxies are fairly bright, and it remains to be determined whether our agreement would be as good for much fainter galaxies.

3.3 Stellar masses

We calculate stellar masses for our galaxies within our global H_{160}-selected sample through the use of our optical+NIR photometry using our own stellar mass code. The method we use to measure stellar masses involves fitting the photometric points, based on a given redshift, to simulated magnitudes based on different star formation histories and constructing a distribution of likely stellar masses, as well as other parameters such as rest-frame optical colours, ages of the stellar population, metallicity, dust extinction and so on. While these non-stellar mass parameters are degenerate, the stellar mass in these calculations is robust (Sawicki & Yee 1998; Papovich, Dickinson & Ferguson 2001; Shapley et al. 2001; Bundy et al. 2006). We fit the photometric redshifts independently of the stellar mass, as our methods for photometric redshifts are likely as accurate as can be measured using limited templates and to have one less free parameter when measuring the stellar masses.

In detail, the basic stellar mass fitting method consists of fitting a grid of model SEDs constructed from BC03 stellar population synthesis models, with different star formation histories. We use an exponentially declining model to characterize the star formation history, with various ages, metallicities and dust contents used for different models. These models are parametrized by an age and an e-folding time for parametrizing the star formation history (τ) and star formation rate (ψ) such that

$$\psi(t) \sim \psi_0 \times \exp(-t/\tau).$$

The values of τ are uniformly selected from a range between 0.01 and 10 Gyr, while the age of the onset of star formation ranges from 0 to 10 Gyr. The metallicity ranges from $Z = 0.0001$ to 0.05 (BC03), and the dust content is parametrized by τ_v, the effective

V-band optical depth, for which we use values $\tau_v = 0.0$, 0.5, 1 and 2. Although we vary several parameters, the resulting stellar masses from our fits do not depend strongly on the various selection criteria used to characterize the age and the metallicity of the stellar population (e.g. Bundy et al. 2006, 2008; Papovich et al. 2006; Conselice et al. 2007a).

It is important to realize that these parametrizations are fairly simple, and it remains possible that stellar mass from older stars is missed under brighter, younger, populations or from an incorrect star formation parametrization. For example, Papovich et al. (2010) find that galaxies are increasing in their star formation rate at $z > 2$, although Papovich et al. (2010) find that this increases measured masses by a factor of 1.6 at most. Furthermore, while the majority of our systems are red galaxies, it is possible that up to a factor of 2 in stellar mass is missed in any star-bursting blue systems. However, stellar masses measured through our technique are roughly the expected factor of 5 to 10 times smaller than dynamical masses at $z \sim 1$, using a sample of disc galaxies (Conselice et al. 2005), demonstrating their inherent reliability to within a factor of 2, similar to the estimated errors based on fitting (Bundy et al. 2006). Our method is also the same as that used to trace the evolution of massive galaxies at lower redshifts $z < 2$ (e.g. Bundy et al. 2006; Conselice et al. 2007a). Our masses also agree with results from multiple methods of measuring stellar masses for the same galaxies (Yan et al. 2004; Papovich et al. 2006; Daddi et al. 2007).

We fit the magnitudes derived from these model star formation histories to the actual data to obtain a measurement of stellar masses using a Bayesian approach. We calculate the likely stellar mass, age and absolute magnitudes for each galaxy at all star formation histories and determine stellar masses based on this distribution. Distributions with larger ranges of stellar masses have larger resulting uncertainties. Typical errors for our stellar masses are 0.2 dex from the width of the probability distributions. There are also systematic uncertainties from the choice of the initial mass function (IMF). Our stellar masses utilize the Salpeter IMF. There are additional random uncertainties due to photometric errors. The resulting stellar masses thus have a total random error of 0.2–0.3 dex, roughly a factor of 2.

There is also a question as to whether or not our stellar masses are overestimated because of the use of the BC03 models. It has been argued by Maraston (2005), among others, that a refined treatment of thermal-pulsating asymptotic giant branch (TP-AGB) stars in the BC03 models results in stellar masses that can be too high by a factor of a few. While we consider an uncertainty of a factor of 2 in our stellar masses, it is worth investigating whether or not our sample is in the regime where the effects of a different treatment of AGB stars, as in e.g. Maraston (2005), will influence our mass measurements. This has been investigated in Maraston (2005) who have concluded that galaxy stellar masses computed with an improved treatment of AGB stars are roughly 50–60 per cent lower.

However, the effect of TP-AGB stars is less important at the rest-frame wavelengths we probe than at longer wavelengths, especially in the rest-frame IR. Since the GNS is H_{160}-band selected, and the observed H_{160} band is used as the flux in which stellar masses are computed, the rest-frame wavelength probed is roughly ~ 0.5 μm at $z \sim 2$. At this wavelength, the effects of TP-AGB stars are minimized, as shown in previous work using the same type of data and the same stellar mass code (Conselice et al. 2007a). To test this on our galaxy sample, we utilized the newer Bruzual & Charlot (in preparation) models, which include an improved TP-AGB star prescription. From this, we find on average that stellar masses are smaller by <0.07 dex using the newer models. At most, the influence of TP-AGB stars will decrease our stellar masses by 20 per cent. The effect of this would reduce the number of galaxies within our sample, particularly those close to the $M_* = 10^{11}\,M_\odot$ boundary. This systematic error is however much smaller than both the stellar mass error we assume (0.3 dex) and the cosmic variance uncertainties (e.g. Conselice et al. 2007a), and thus we conclude that it is not a significant factor within our analysis. The stellar mass versus redshift relation for our sample is shown in Fig. 7. We analyse the stellar mass function in detail in Mortlock et al. (in preparation), including how photometric redshift and stellar mass uncertainties affect the stellar mass function up to $z \sim 3.5$, although we give an initial analysis of the number densities for massive galaxies with $M_* > 10^{11}\,M_\odot$ later in this paper (Section 4.3.3).

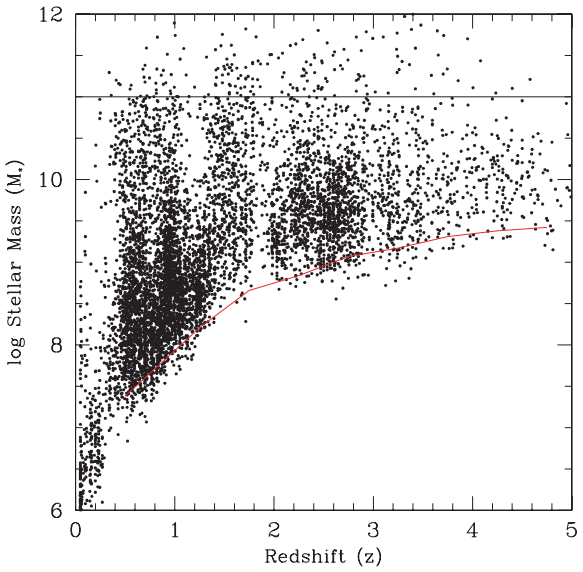

Figure 7. The distribution of redshifts and stellar masses for our H_{160}-selected GNS galaxies. The red solid line shows the evolution of the minimum stellar mass we could detect at our H_{160}-band depth as a function of redshift for a maximally old stellar population. The solid horizontal line shows the $\log M_* > 11$ limit in which the primary sample for selection of the GNS galaxies was carried out. The slight gap near $z \sim 2$ is only present for galaxies with stellar masses lower than the limit we consider in this paper, and there is no systematic property associated with it.

4 ANALYSIS

4.1 Massive galaxy selection

The selection of massive galaxies at high redshift is an important process which remains difficult due to the inability to easily acquire spectroscopic redshifts for a sizeable population of galaxies at high redshifts. This is also different from selection done through star formation rates or morphology, such as an early-type galaxy selection (Stanford et al. 2004). At lower redshifts ($z < 1.4$), it is fairly straightforward to obtain redshifts through spectroscopic surveys such as DEEP2 or VVDS, combined with deep NIR imaging to measure stellar masses (e.g. Bundy et al. 2006; Conselice et al. 2007a).

As described in our selection method for the GNS fields, there are a few approaches for determining the massive galaxy population at high redshifts. These methods typically use a colour selection of some form, ranging over wavelengths from the U band to the IR with *Spitzer*, which generally locate the Lyman break through the use of deep U-band data or the Balmer and 4000-Å breaks

through IR+optical filters. However, it has never been shown that a complete sample of massive galaxies can be selected through these methods and it remains possible, or even likely, that many massive galaxies are missed by not having a colour or magnitude which fits the criteria being selected for (see Section 2.2). For example, ultradusty galaxies would possibly have SEDs that would not be included in our selection.

As discussed in Section 2.2, the methods for initial galaxy selection that we use in this paper for our primary target selection include the BzK method (Daddi et al. 2004), the IERO method (Yan et al. 2004), the DRG method (Franx et al. 2003; Papovich et al. 2006) and the BX/BM method (Reddy et al. 2008). In this section, we give a description of the relationship between these different methods for determining the population of massive galaxies at redshifts $z > 2$. This has been done previously for other populations at high redshift by Reddy et al. (2005) and Grazian et al. (2007).

A graphical summary of the distribution in redshift for the colour-selection methods for our massive galaxies is shown in Fig. 8 and the distribution of stellar masses in Fig. 9 using the initial selection described in Section 2.2. As can be seen in these figures, there is a slight, but insignificant, difference in the redshifts and stellar mass selection for these massive galaxies.

We find that the BzK-selected massive galaxies tend to lie towards the lower range of redshifts, with an average in GOODS-N of $\langle z \rangle = 2.12 \pm 0.28$ and in the GOODS-S of $\langle z \rangle = 2.17 \pm 0.33$. On the other hand, the IEROs have a higher average redshift range, with

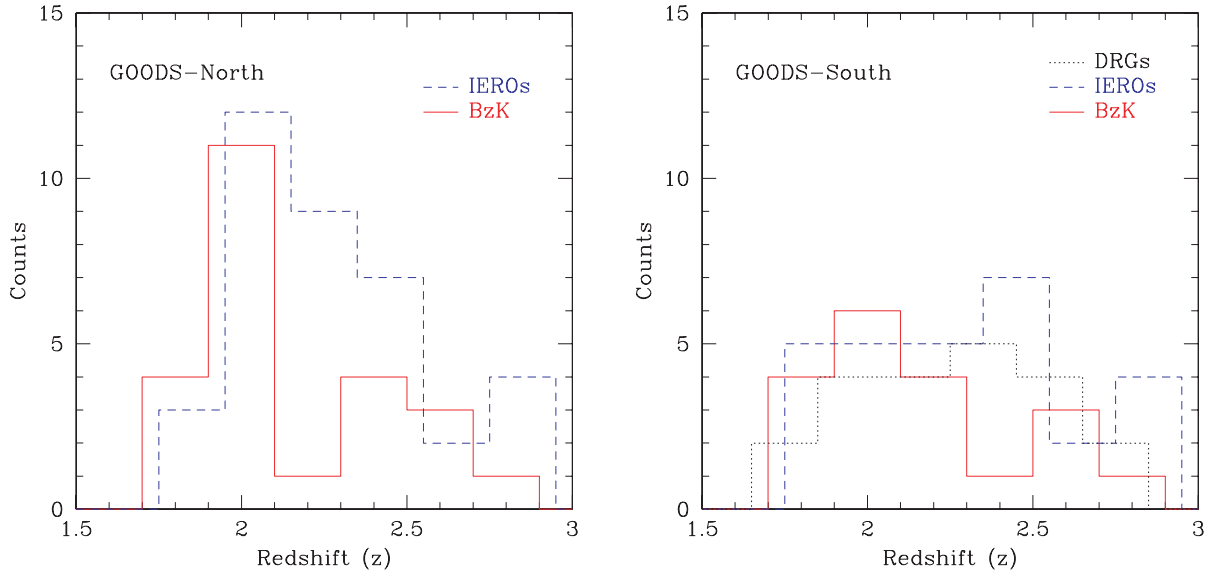

Figure 8. The redshift distribution of galaxies of different types. Shown in the left-hand panel are the redshift distributions for the IEROs and BzKs denoted by dashed and solid lines, respectively, for the GOODS-N field. The right-hand panel shows a similar trend, except it also includes the DRG-selected galaxies. Note that if an object is selected by multiple methods, that galaxy is plotted for each type to which it belongs. It appears that the IEROs are selected from a slightly higher redshift population than the BzK galaxies.

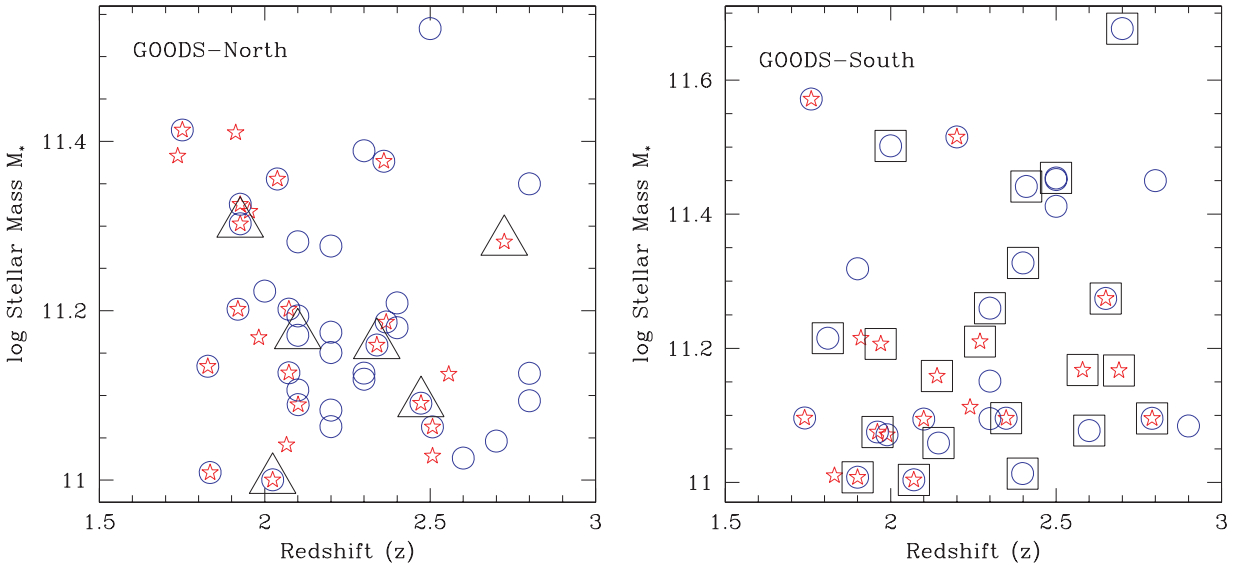

Figure 9. The distribution of our initial sample of BzKs, IEROs, DRGs and BM/BX objects from which our selection of NICMOS fields was made. The left-hand panel shows the distribution within GOODS-N, while the right-hand panel shows this within GOODS-S. The symbols are as follows: stars are BzKs; open circles are IEROs; boxes are DRGs which are only found in GOODS-S and triangles are BM/BX objects, which are only located within GOODS-N.

$\langle z \rangle = 2.24 \pm 0.28$ in the North and $\langle z \rangle = 2.29 \pm 0.34$ in the South. The DRGs tend to be selected at an even higher redshifts than either the BzKs or IEROs, with an average value of $\langle z \rangle = 2.32 \pm 0.29$ in GOODS-S. However, we find that all three methods find galaxies of similar mass, with the average stellar mass for each type $\langle M_* \rangle \sim 2 \times 10^{11}\,\mathrm{M}_\odot$, and all methods give a similar relatively large range in redshifts.

Furthermore, as can be seen by the different symbols in Fig. 9, there are many massive systems which are selected by more than one method. In fact, we find that nearly all selection methods overlap with each other in terms of the galaxies selected. Only a small fraction of our systems are selected by just one method, with the IERO selection being the most likely method for finding unique galaxy samples.

The breakdown of our selections is such that over all massive galaxies in GOODS-N, 24 objects, or 53 ± 11 per cent, of the systems are selected by the BzK method. The corresponding number is 18 systems, or 51 ± 12 per cent, of those in the GOODS-S field. The IERO selection is the most efficient for identifying our massive galaxy sample. In the GOODS-N, we find that 37 galaxies, or 82 ± 0.14 per cent, are located as IEROs, while in GOODS-S, with 27 systems the fraction is 66 ± 0.15 per cent. In the GOODS-S where we are able to use the DRG method, we find that a total of 21 galaxies, or 77 ± 0.14 per cent, in our massive galaxy sample are selected. Finally, we note that only a small fraction of our sample of massive galaxies in the GOODS-N at $1.7 < z < 2.9$ are detected through the BM/BX-selection method (Reddy et al. 2008; Fig. 9). Every massive galaxy at our redshift range of interest detected as a BM/BX is also detected as either an IERO (six out six systems) or as a BzK (five out of six systems).

There are however a few biases which can produce some of these results. The first is that the BzK method, as described in Section 2.2, is limited to $K_{\mathrm{Vega}} = 22.0$ and 20.5 in the GOODS-S and GOODS-N, respectively. The method will not find bluer galaxies near $z \sim 3$, which will drop out of the sample at around $z \sim 2.5$. However, according to Daddi et al. (2004, equation 6), we will be largely complete in mass of $M_* > 10^{11}\,\mathrm{M}_\odot$ at $z < 2.5$ – through most of our redshift range. Furthermore, the IERO selection is potentially the most successful in this experiment due to the depth of the IRAC imaging compared to the *K*-band data used in the DRG and BzK methods. Furthermore, the blunt colour selection for the IEROs will find more objects although it remains possible that there are also more false positives with this method of colour selection. We however conclude that no one single method for locating distant massive galaxies can be used to find complete samples and that either a combination of different methods or a photometric-redshift-selected sample is essential.

4.2 Stellar mass distribution

In this section, we investigate the stellar masses which we compute based on our H_{160}-band detections matched with our ACS imaging. These stellar masses are computed as described in Section 3.3. This allows us both to examine the distribution of the stellar masses which we measure for the GNS sample and to test the differing methods outlined in Section 2.2 for selecting high-redshift galaxies. These stellar masses will be the focus of a detailed analysis in Mortlock et al. (in preparation).

We present in Fig. 7 the stellar mass distribution of our sample out to $z \sim 5$. We also show in this figure the stellar mass of a maximally old stellar population which would still be detected at each redshift. Note that there is a slight gap near redshift $z \sim 1.8$ which is likely partially the result of photometric redshift systematic errors. This gap however is also quite small, roughly $\delta z = 0.05$ in size, and there is no dependence of stellar mass or colour in the galaxies that are within this gap.

We use our new measured masses to determine the completeness and ability of colour-selection methods to find the highest mass galaxies at $z > 2$. As we are using a heterogeneous selection for our initial high-mass colour-selected sample, it is important to carry out this comparison to determine how and whether a stellar mass selected sample using redshifts is similar to a colour-selected one, and if different, how.

We find in our new photometric redshift/mass H_{160}-based catalogue, independent of our original colour-selection catalogue (Section 2.2), that between $1.7 < z < 2.9$ there are 75 massive galaxies within our criteria of $M_* > 10^{11}\,\mathrm{M}_\odot$ using our new *BVizH* stellar masses and photometric redshifts. Nearly all of these galaxies are selected by the colour methods for finding high-redshift massive galaxies (Section 2.2), thereby showing that we have a nearly complete sample of massive galaxies at high redshift, sans systems that are extremely dusty that would not be measured with our photometric redshifts accurately. The reason there is a slight difference from our 80 original galaxies is that the computation of photometric redshifts and stellar masses from our H_{160}-band-selected catalogue are slightly different from those which were used to construct the original catalogue. Overall, if we consider a slightly wider stellar mass and redshift range, we are able to recover all but 10 of the systems which were originally suggested by our initial colour-selected analysis (Section 2.2) to be within our stellar mass and redshift range of interest. Although we find that some galaxies are not selected by our methods, these are likely to be systems which just missed our initial criteria based on our strict stellar mass and photometric redshift cut.

Overall, we find that the average stellar mass difference between our originally estimated stellar masses, from the colour-selected samples, and our new calculations, is 0.03 dex, with a larger scatter of 0.39 dex. This is slightly larger than our 0.2-dex random error measurement, and this is the result of differing redshifts between the two samples. This difference is furthermore reduced to 0.29 dex in scatter when we examine galaxies for which the two redshift estimates are within $\delta z = 0.1$ of their pre-redshift and post-redshift measures.

In other words, when we examine only those galaxies for which both redshift estimates are near to each other, we find a much smaller difference between the measured stellar masses. The differences in the stellar masses can be explained therefore by the fact that the redshifts are different between the two samples. We furthermore find that the photometric redshift measures for our massive galaxy sample from our original catalogue compared with the new measures from the H_{160}-band-selected sample are $\delta z/(1+z) = 0.05$, slightly higher at $z > 2$ (Section 3.2) – similar to the quality of our overall photometric redshift quality when compared to the measured spectroscopic redshifts.

4.3 Properties of massive galaxies at $z > 2$

4.3.1 Previous investigations

One of the major focuses of the GNS is to examine the properties of massive galaxies at $z > 2$. In the past, this type of analysis has generally been performed at lower redshifts, at $z < 2$, where properties of the massive galaxy population are now well described (e.g. Conselice et al. 2007a,b; Trujillo et al. 2007; Bundy et al. 2008;

Foucaud et al. 2010). Examining the galaxy population at higher redshifts is more challenging due to the fact that spectroscopic redshifts are difficult to obtain for a sizeable fraction of galaxies. However, some early attempts have been performed which suggest that significant information is obtainable through deep spectroscopy of distant massive galaxies (e.g. Kriek et al. 2008).

Despite the lack of spectroscopic redshifts for our sample, we can still make progress using photometric redshifts and stellar mass measures, which have already been used in many papers for understanding the evolution of the massive galaxy population at higher redshifts. While we do not provide a detailed analysis of the massive galaxy population at $z > 2$ within this paper, we give some basic features as well as provide information that will be used in other papers that follow this one in terms of the analysis of these distant galaxies.

We have previously published an analysis of the size evolution of massive galaxies using this same data (e.g. Buitrago et al. 2008), finding that the sizes of our massive galaxy sample are much smaller by a factor of 2–5 compared with similar stellar mass selected galaxies in today's Universe. Tables 5 and 6 list the morphological

Table 5. Structural parameters for galaxies with $M_* > 10^{11}$ M$_\odot$ within the GOODS-N field.

ID	R_e [a] (arcsec)	Sérsic n [a]	b/a	PA (°)	$\mu_{\rm eff}$ (mag arcsec^{-2})	$z_{\rm spec}$	sep (arcsec)	$z_{\rm phot}$
43	0.14 ± 0.00	1.67 ± 0.05	0.75	50.6	17.26	–	–	1.56
77	0.35 ± 0.01	1.35 ± 0.03	0.75	−23.9	18.82	–	–	1.71
21	0.14 ± 0.01	1.0 ± 0.20	0.38	9.6	16.92	–	–	2.47
227	0.25 ± 0.00	2.39 ± 0.05	0.73	−41.3	18.00	–	–	1.79
373	0.27 ± 0.01	0.61 ± 0.03	0.26	−17.3	16.63	–	–	2.53
552	0.44 ± 0.01	2.36 ± 0.05	0.82	77.2	18.57	–	–	1.81
730	0.58 ± 0.01	0.48 ± 0.02	0.47	28.2	19.03	–	–	2.11
840	0.14 ± 0.00	2.38 ± 0.09	0.49	17.4	16.63	–	–	2.14
856	0.17 ± 0.00	3.63 ± 0.10	0.71	−17.8	17.63	–	–	1.82
999	0.20 ± 0.00	1.28 ± 0.03	0.68	64.3	16.86	–	–	1.47
1144	0.49 ± 0.01	1.35 ± 0.03	0.32	−24.0	18.58	–	–	2.66
1129	0.32 ± 0.01	0.17 ± 0.04	0.69	−8.7	18.81	–	–	2.77
1257	0.09 ± 0.00	3.45 ± 0.20	0.73	−7.3	17.04	–	–	1.66
1394	0.30 ± 0.00	1.15 ± 0.03	0.57	−83.4	18.16	–	–	2.14
1533	0.33 ± 0.03	1.21 ± 0.25	0.91	−82.3	20.11	–	–	0.66
1666	0.61 ± 0.01	0.57 ± 0.01	0.63	5.7	18.35	1.76	0.35	2.36
1768	0.14 ± 0.01	2.05 ± 0.16	0.60	−78.6	16.90	–	–	2.10
1826	0.35 ± 0.03	3.95 ± 0.28	0.69	15.2	19.30	1.993	0.40	1.93
1942	0.31 ± 0.01	1.99 ± 0.26	0.91	−4.1	18.02	–	–	2.05
2066	0.21 ± 0.01	1.62 ± 0.17	0.70	46.6	17.71	2.91	0.35	2.02
2083	0.12 ± 0.00	4.04 ± 0.18	0.53	−3.0	16.07	–	–	1.93
2049	0.17 ± 0.02	2.45 ± 0.50	0.54	−75.3	17.61	–	–	2.44
2282	0.57 ± 0.03	0.76 ± 0.06	0.59	80.1	20.20	–	–	2.11
2411	0.54 ± 0.01	0.56 ± 0.03	0.74	−21.9	19.67	–	–	2.18
2564	0.11 ± 0.00	1.69 ± 0.07	0.47	−27.9	16.31	–	–	1.80
2734	0.21 ± 0.01	1.60 ± 0.21	0.77	−14.5	18.54	–	–	2.11
2678	0.11 ± 0.00	2.39 ± 0.09	0.35	−74.6	15.17	–	–	2.06
2764	0.29 ± 0.01	1.01 ± 0.09	0.84	−52.7	18.85	–	–	1.98
2902	0.22 ± 0.01	1.88 ± 0.18	0.50	−15.7	18.46	–	–	2.02
2837	0.35 ± 0.00	0.35 ± 0.02	0.42	12.3	17.92	1.79	0.30	1.72
2965	0.15 ± 0.00	1.70 ± 0.11	0.62	−57.9	16.74	–	–	3.03
3036	0.20 ± 0.00	2.15 ± 0.10	0.50	−31.9	17.41	–	–	1.66
3126	0.36 ± 0.01	1.27 ± 0.07	0.57	62.4	19.35	–	–	1.84
3250	0.34 ± 0.01	0.34 ± 0.04	0.27	27.9	17.71	–	–	2.10
3422	0.35 ± 0.02	0.50 ± 0.00	0.37	−64.4	18.13	–	–	2.16
3387	0.05 ± 0.00	2.50 ± 0.00	0.63	−57.8	15.65	–	–	1.76
3582	0.27 ± 0.02	1.92 ± 0.37	0.77	74.6	19.33	–	–	2.34
3629	0.19 ± 0.00	1.40 ± 0.04	0.70	47.5	16.94	–	–	2.16
3818	0.40 ± 0.00	2.07 ± 0.03	0.79	−21.4	18.98	–	–	1.62
3766	0.28 ± 0.00	1.79 ± 0.06	0.77	−40.1	18.23	–	–	2.12
3822	0.21 ± 0.01	2.33 ± 0.23	0.84	−45.3	19.04	–	–	2.33
3970	0.26 ± 0.02	3.67 ± 0.36	0.59	−5.1	18.60	–	–	2.17
4121	0.06 ± 0.00	2.20 ± 0.00	0.34	−74.3	14.17	–	–	4.38
4033	0.54 ± 0.01	1.28 ± 0.02	0.54	−2.6	18.65	–	–	1.92
4239	0.38 ± 0.02	1.20 ± 0.09	0.52	−42.5	19.05	–	–	1.87

[a]The values of the errors on R_e and Sérsic n are representative of the 1σ model errors from GALFIT (see Buitrago et al. 2008). This does not take into account many possible sources of error that may bias these measurements, including magnitude of galaxy, concentration of its light profile, etc. The uncertainty in these structural parameters increase by of the order of 10 per cent for R_e and 20 per cent for n due to changes in the PSF across the NICMOS NIC3 field of view. Also listed is the fitted axial ratios for these galaxies (b/a) and PA. The effective surface brightness ($\mu_{\rm eff}$) is listed, as is the spectroscopic redshift ($z_{\rm spec}$), if available. The value of 'sep' is the difference between the position of an object and the identification of the spectroscopic target, in arcsec. Finally, the calculated photometric redshift, $z_{\rm phot}$, is shown.

Table 6. Structural parameters for galaxies with $M_* > 10^{11}$ $M_\odot$ within the GOODS-S field.

ID	R_e [a] (arcsec)	Sérsic n[a]	b/a	PA (°)	μ_{eff} (mag arcsec^{-2})	z_{spec}	sep (arcsec)	z_{phot}
4299	0.31 ± 0.01	0.65 ± 0.06	0.46	−8.0	18.57	–	–	0.31
4281	0.20 ± 0.02	3.03 ± 0.57	0.57	−39.8	18.61	–	–	1.70
4348	0.34 ± 0.02	1.78 ± 0.17	0.58	85.3	19.84	–	–	0.76
4434	0.13 ± 0.00	1.35 ± 0.05	0.67	−71.4	16.56	2.09	0.12	1.96
4399	0.08 ± 0.01	3.40 ± 1.00	0.70	−69.9	17.70	–	–	2.31
4557	0.34 ± 0.01	1.48 ± 0.05	0.38	72.6	17.45	–	–	1.75
4754	0.38 ± 0.01	0.75 ± 0.03	0.44	−37.6	18.68	–	–	2.21
4706	0.06 ± 0.00	4.62 ± 0.19	0.50	−75.7	14.69	2.34	0.08	1.77
4882	0.10 ± 0.00	2.25 ± 0.08	0.65	2.8	16.44	–	–	1.41
4941	0.24 ± 0.16	3.79 ± 4.42	0.80	−22.8	18.42	–	–	2.87
5171	0.10 ± 0.00	3.36 ± 0.28	0.66	−32.0	16.50	2.40	0.21	2.58
5281	0.48 ± 0.01	1.14 ± 0.02	0.70	16.1	19.03	–	–	0.69
5445	0.42 ± 0.03	1.06 ± 0.08	0.52	61.7	19.36	–	–	2.39
5372	0.20 ± 0.02	1.64 ± 0.22	0.42	−32.2	17.63	–	–	2.53
5533	0.09 ± 0.00	3.20 ± 0.32	0.63	−33.5	16.29	–	–	2.37
5524	0.06 ± 0.00	1.00 ± 0.06	0.19	−22.8	12.48	–	–	2.82
5764	0.16 ± 0.01	2.88 ± 0.15	0.64	−27.6	16.95	–	–	2.34
5853	0.24 ± 0.01	0.38 ± 0.05	0.49	−84.0	17.78	2.41	0.16	1.85
5933	0.27 ± 0.00	1.08 ± 0.05	0.92	64.0	18.84	–	–	2.48
6035	0.22 ± 0.01	4.27 ± 0.19	0.83	−67.9	18.19	–	–	2.75
6114	0.11 ± 0.00	3.90 ± 0.12	0.72	−68.4	16.00	–	–	1.55
6220	0.40 ± 0.01	1.45 ± 0.05	0.80	−73.5	19.57	–	–	1.55
6352	0.50 ± 0.03	2.59 ± 0.11	0.51	65.7	19.54	–	–	2.56
6468	0.31 ± 0.01	0.98 ± 0.04	0.46	−44.8	17.45	–	–	1.76
6584	0.34 ± 0.01	1.10 ± 0.03	0.22	68.8	17.16	–	–	1.66
6575	0.41 ± 0.01	0.33 ± 0.02	0.73	−62.6	18.30	–	–	1.52
6876	0.29 ± 0.01	0.47 ± 0.04	0.35	−82.7	17.18	–	–	1.35
7090	0.37 ± 0.01	2.68 ± 0.06	0.50	−65.7	17.89	–	–	2.58
7155	0.10 ± 0.01	4.52 ± 0.35	0.51	−66.8	15.67	–	–	0.49
7320	0.12 ± 0.00	1.12 ± 0.05	0.56	−31.6	16.18	–	–	1.39
7425	0.16 ± 0.00	2.13 ± 0.06	0.45	66.4	16.48	1.31	0.2	1.40
7677	0.21 ± 0.00	2.85 ± 0.09	0.83	50.0	17.01	1.19	0.15	1.34
7970	0.37 ± 0.01	0.56 ± 0.02	0.84	−79.4	18.73	–	–	1.72
8140	0.19 ± 0.00	2.72 ± 0.07	0.77	−19.8	17.24	1.90	0.14	1.78
8213	0.15 ± 0.00	1.69 ± 0.07	0.63	53.8	16.56	–	–	0.70

[a]The values of the errors on R_e and Sérsic n are representative of the 1σ model errors from GALFIT (see Buitrago et al. 2008). This does not take into account many possible sources of error that may bias these measurements, including magnitude of galaxy, concentration of its light profile, etc. The uncertainty in these structural parameters increases by of the order of 10 per cent for R_e and 20 per cent for n due to changes in the PSF across the NICMOS NIC3 field of view. Also listed is the fitted axial ratios for these galaxies (b/a) and PA. The effective surface brightness (μ_{eff}) is listed, as is the spectroscopic redshift (z_{spec}), if available. The value of 'sep' is the difference between the position of an object and the identification of the spectroscopic target, in arcsec. Finally, the calculated photometric redshift, z_{phot}, is shown.

properties of our original 80-galaxy sample. These include the GALFIT values of the Sérsic index (n) and the effective radii (R_e), and other shape measures such as the position angle (PA), axial ratio (b/a), effective surface brightness as well as the photometric and spectroscopic redshifts for these systems.

Using this data set combined with previous work at lower redshifts (e.g. Trujillo et al. 2007; Cassata et al. 2010), we find that there is a gradual increase in the sizes of galaxies when viewed at lower redshifts. Understanding how these galaxies become larger at lower redshifts is one of the primary focuses of studies of massive galaxies, and a solution to this problem remains outstanding.

Another issue we have used this data set to address is the merger history of these massive galaxies at $z < 3$ (Bluck et al. 2009; Bluck et al., in preparation). By investigating pairs of galaxies at these redshifts, we find that the merger fraction for massive galaxies contains a steep decline, which falls as $\sim(1 + z)^3$, and that overall there are no more than roughly two or three major mergers occurring for these massive galaxies at $z < 3$, suggesting that at most the stellar mass is tripled by such mergers, and that furthermore, these mergers are probably not directly producing the increase in the sizes of these massive galaxies (e.g. Buitrago et al. 2008). This is further confirmed when examining similar results at lower redshifts (Conselice et al. 2009). We are currently investigating the merger history of GNS galaxies through the use of the CAS morphological parameters using the NICMOS imaging (e.g. Conselice et al. 2008b; Bluck et al. 2011).

We are also investigating the star formation history for these systems by using MIPS photometry and rest-frame ultraviolet (UV) fluxes (Bauer et al. 2011; Weinzirl et al., in preparation). Furthermore, we are looking at the environmental properties of our galaxies and are comparing their environments to similar mass galaxies at lower redshifts (e.g. Grützbauch et al. 2011b). We are also investigating the surface brightness profiles and Kormendy relations and minor merger histories for these galaxies (Bluck et al. 2011) and how, by comparing these measurements to simulations of nearby galaxies placed at high redshift, the evolutionary history of these

galaxies can be deciphered (e.g. Conselice et al., in preparation). Finally, we are investigating the more general mass-selected population at high redshift through the evolution of stellar mass functions and colours (e.g. Mortlock et al., in preparation).

4.3.2 Colours

The colours of our massive galaxies are typically quite red, and most of them have colours $(z - H) > 1.5$ (Figs 10 and 11) and with H_{160} magnitudes $H_{160} \sim 23$ AB mag. In Figs 10 and 11, the original colour-selected massive sample is shown by the open stars. The objects within our new photometric redshift selection which are not within the original sample also fall within this area of red colour space, as denoted by the open blue squares (Figs 10 and 11). This also shows that these galaxies are largely very faint in the optical and that the best way to study them is in the NIR. However, as can be seen through the blue squares in Fig. 10, some fraction of the systems which are selected by the photometric redshift technique have bluer colours, with flat spectrum colours of $(z - H) \sim 0$. These galaxies would not have been selected through our colour techniques due to the fact that such systems are too blue and thus are hard to distinguish from lower redshift galaxies. However, as we will see, these objects are not a dominant part of the population, and in fact most of the global quantities calculated for these massive galaxies at $z > 2$ are largely the same whichever of these two methods (redshifts or colour) for selection is used.

We can also get some basic idea of the star formation history and stellar populations of these massive galaxies by examining their position in colour–colour space (Fig. 11) and their location within rest-frame colour–magnitude diagrams (Fig. 12). We only show galaxies down to $M_* = 10^{10}\,\mathrm{M}_\odot$ on these colour–magnitude diagrams, where we are complete in our selection of galaxies. What we find is that our massive galaxies span a range in $(B - z)$ colour, but are all fairly red in $(z - H)$, with values larger than $(z - H) = 2$

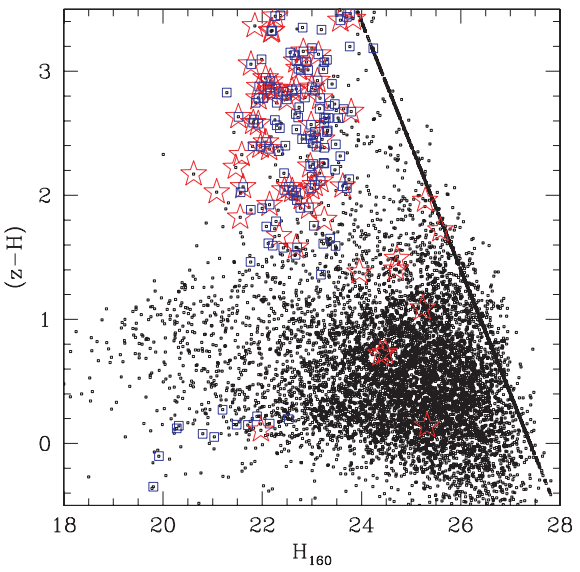

Figure 10. The H_{160} band versus $(z - H)$ colour diagram for our H_{160}-band-selected sample. Shown here, as red open stars, are the locations of our initial stellar mass selected sample, and the blue boxes are those selected through photometric redshifts at the same mass and redshift ranges. As can be seen, many of the massive galaxies in our sample are quite red. The apparent line on the right of the diagram is the result of galaxies which are undetected in the z band.

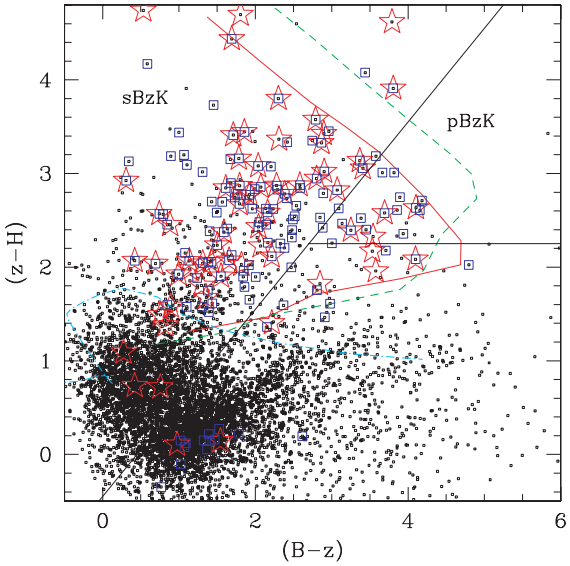

Figure 11. The $(z - H)$ versus $(B - z)$ diagram for the H_{160}-band-selected galaxies in our sample. The red stars show the location of our initial massive galaxy sample based on colour selections (Section 2.2), while the blue squares show the location of massive systems with $M_* > 10^{11}\,\mathrm{M}_\odot$ at $1.8 < z < 3.0$ identified through photometric redshifts. The various lines on this figure show the change in colour for simple single stellar populations of a given age as observed at various redshifts. Changes in colour seen for these models are purely due to redshift effects. The cyan dot–dashed line shows the evolution of a 100-Myr single stellar population from redshifts of $z = 0$ to 3.8. The green dashed line shows a 2.5-Gyr single stellar population as observed at redshifts from $z = 0$ to 2.6, while the red solid line shows a 11-Gyr-old stellar population as viewed from $z = 0$ to 2.2.

for most systems. We find that a large fraction of our massive galaxy systems are within the star-forming region of the BzK diagnostic plots (e.g. Daddi et al. 2007; Lane et al. 2007) after converting the diagnostics to a BzH selection using a typical colour of $(H - K) \sim 0.25$ for a galaxy at $z \sim 2$. This implies that within this selection, there are a significant number of galaxies with enough observed B-band flux to be considered star-forming systems (see also Bauer et al. 2011). The lines in Fig. 11 furthermore show where various single stellar populations would lie in this parameter space whose colours are affected simply by k-corrections.

We furthermore use the redshifts and magnitudes of our galaxies to calculate rest-frame $(U - B)$ colours, which are directly compared with colours from lower redshift galaxies of similar masses (e.g. Conselice et al. 2007a). The result of this rest-frame $U - B$ versus M_B diagram is shown in Fig. 12, where we have divided up our sample into ultramassive galaxies with $M_* > 10^{11.5}\,\mathrm{M}_\odot$, medium-mass galaxies with $10^{11.5}\,\mathrm{M}_\odot > M_* > 10^{11}\,\mathrm{M}_\odot$ and those systems with more modest, but still relatively high masses, with $10^{11}\,\mathrm{M}_\odot > M_* > 10^{10}\,\mathrm{M}_\odot$. We also show this evolution in colour–magnitude for our galaxies divided into different redshift bins. Note that we are complete for $M_* > 10^{11}\,\mathrm{M}_\odot$ galaxies up to $z = 3$. The blue and red lines in Fig. 12 show the demarcation between the red sequence and the blue cloud, and the location of the red sequence as seen at lower redshifts (Faber et al. 2007). These lines are evolved passively from lower redshift to higher-z.

What one can see immediately from Fig. 12 is that most of the massive galaxies, which tend to be also bright, are near or close to the red sequence, while the lower mass galaxies are more often bluer systems, with in fact, very few of the galaxies with lower masses in our sample within the red sequence. The bimodality is particularly

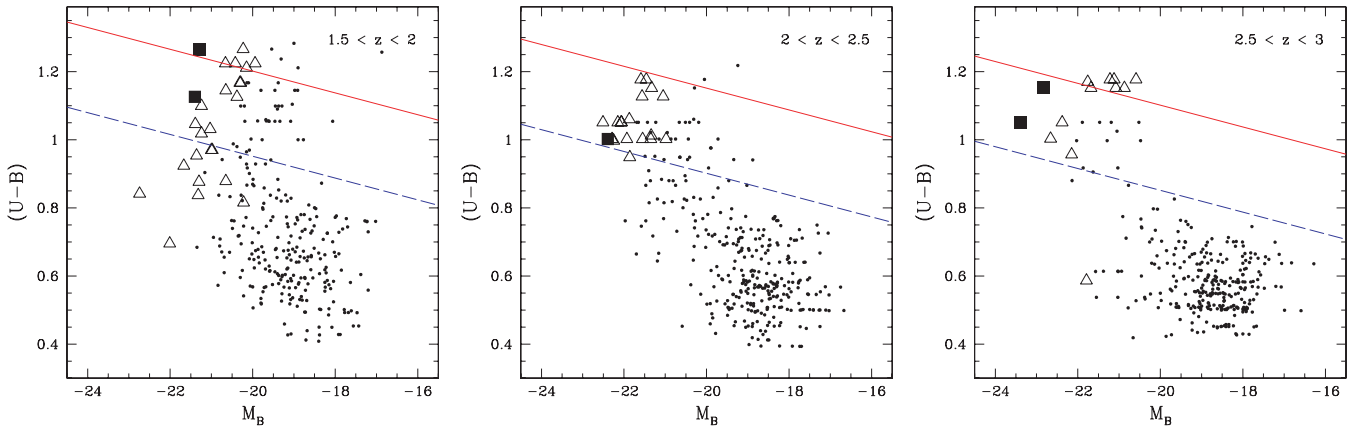

Figure 12. Colour–magnitude diagram in rest-frame units for our sample of galaxies. Shown are the data plotted in different ways depending on their stellar mass. The most massive galaxies with $M_* > 10^{11.5}\,M_\odot$ are shown as solid squares, those at $10^{11}\,M_\odot < M_* < 10^{11.5}\,M_\odot$ are shown as open triangles, and the dots are for those galaxies with stellar masses $M_* < 10^{11}\,M_\odot$. The red solid line is the red sequence as determined by Faber et al. (2007), while the blue dashed line shows the separation at which galaxies are considered to be within the blue cloud. Both of these lines are evolved with redshifts for a passively evolving stellar population.

present at $2.5 < z < 3$, where nearly all the massive galaxies with $M_* > 10^{11}\,M_\odot$ are exclusively on the red sequence, while those less massive galaxies are found within the blue cloud. As we go to lower redshift, it appears that some of the massive galaxies are now seen in the blue cloud.

This apparent evolution from the red sequence to the blue cloud is likely due to the fact that the number densities of massive galaxies increases with time, and thus massive galaxies at $1.5 < z < 2.0$ are not the same type of system found at higher redshifts. In other words, the build-up of massive galaxies occurs by adding bluer galaxies, that were formerly lower mass earlier, to the high-mass bin. Furthermore, as discussed in Bauer et al. (2011), the fact that these massive galaxies are red does not necessarily imply that they are 'red and dead', but in fact, that they are undergoing dusty star formation (e.g. Papovich et al. 2006). A detailed discussion of this is presented in Bauer et al. (2011) and Grützbauch et al. (2011b).

4.3.3 *The evolution of massive galaxy number densities*

One of the major ways to examine the evolution of massive galaxies is to investigate how their number densities evolve with time (e.g. Conselice et al. 2007a). Various studies have previously examined how luminosity and mass-selected samples have evolved over redshift. A very popular way to do this is by examining galaxy luminosity functions, typically in the B band, and to fit the distribution of luminosities to a Schechter function, giving a characteristic luminosity L^* as well as a faint-end slope (α), and normalization given by the parameter ϕ. Typically one measures evolution in the galaxy population by fitting these parameters and then determining how they have evolved over time. This is useful for determining how the global galaxy population changes or in the case of faint- or low-mass galaxies through examining how the α parameter evolves with redshift.

An alternative approach is to examine galaxies based on a certain luminosity or stellar mass threshold, such as our selection in this paper of $M_* > 10^{11}\,M_\odot$. There are many reasons for believing that stellar mass is a better indicator for tracing the evolution of galaxies than luminosity. One reason is that stellar mass measurements in principle do not depend upon the ongoing star formation rate. A galaxy undergoing a relatively higher star formation rate will appear brighter than a quiescent galaxy with the same stellar mass. However, the star formation rate and resulting mass-to-light ratio for the galaxy can be derived from the SED which can then be accounted for to reveal the true underlying stellar mass of the galaxy. Furthermore, the stellar mass will only increase monotonically with the passage of time, whereas the ongoing star formation rate and luminosity will vary, making them less reliable tags of galaxies over time.

We have also found within the GNS, and at $z < 1$ within the POWIR survey (Conselice et al. 2008a), that stellar mass is the most important quantity for determining the properties of a galaxy, such as its colour and star formation rate (e.g. Grützbauch et al. 2011a,b). There is a strong correlation up to $z \sim 3$, such that we find that galaxies are redder at high stellar masses and bluer at lower stellar masses. This trend stays the same at all redshifts thus far probed, and a similar trend can be seen when considering the star formation rate and the specific star formation rate correlations with stellar mass.

Previously, the number densities of $M_* > 10^{11}\,M_\odot$ galaxies at $z < 2$ were investigated using the POWIR/DEEP2 data set (Conselice et al. 2007a). It was found in this previous paper that the number densities of these massive galaxies, and more specifically, those of masses $>10^{11.5}\,M_\odot$, were largely in place at $z = 1$–1.5, and with a significant number of systems present at $z = 2$. The fact that these massive galaxies already exist in large numbers at these redshifts, suggests that we have to go to higher redshifts to trace the evolution of these systems. This was one reason for carrying out the GNS survey, for which we can make an estimate of the number densities of massive galaxies at even higher redshifts.

We do this in two ways – both by using our original colour-selected sample, and likely slightly inhomogeneous sample, as well as by the use of our newly measured photometric redshifts and stellar masses from our *BVizH*-selected sample (Fig. 13). The errors on this plot result from number counting statistics only.

In Fig. 13, we have down weighted the stellar mass densities at $1.7 < z < 2.9$ to account for the fact that our fields were selected to contain massive galaxies with $M_* > 10^{11}\,M_\odot$. The GNS fields were selected based on having at least one colour-selected massive galaxies at $1.7 < z < 2.9$ in the NIC3 field of view within the GOODS-S and GOODS-N. These fields were however not overselected for

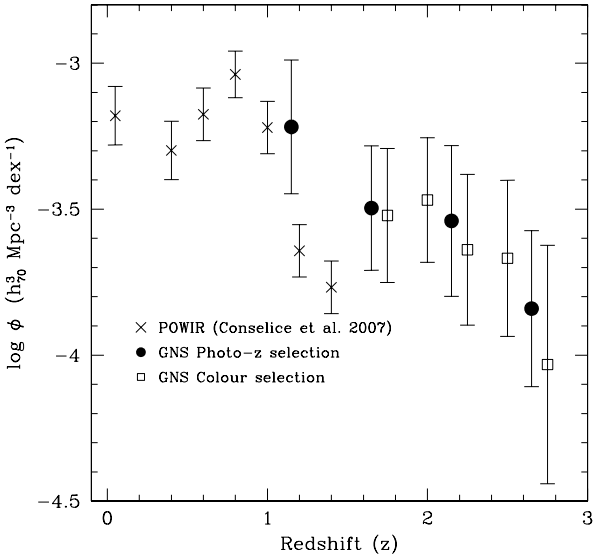

Figure 13. The number density evolution in units of h_{70}^3 Mpc^{-3} for galaxies with stellar masses, $M_* > 10^{11}$ M$_\odot$ as seen within the GNS and within the POWIR survey (Conselice et al. 2007a). We show here the number densities calculated using two different galaxy sample selections, both a photometric redshift method and the original colour-selection method, with both methods showing relatively good agreement.

massive galaxies as a number of other objects (drop-out galaxies, submillimetre galaxies, BM/BX galaxies), as well as lower mass BzKs, DRGs and IEROs, were used to make the final selection.

Ultimately the selection used 80 unique $M_* > 10^{11}$ M$_\odot$ galaxies. We calculate the correction factor for this selection by using the original list of massive galaxies with these redshifts and stellar masses from the colour-selected lists over the entire GOODS fields and calculate how many non-overlapping massive galaxies are there. We find 92 of these systems in the North and 83 in the South. This gives a surface density of 0.58 arcmin^{-2}. The 80 galaxies within the GNS area provides a surface density of 1.77 arcmin^{-2} in the NICMOS pointings. Thus, the ratio of these gives the overdensity for $M_* > 10^{11}$ M$_\odot$ galaxies at $z > 1.7$ and $z < 2.9$ in the NICMOS data, which is a factor of 3.05, which we use to down weight the number densities we calculate for the $M_* > 10^{11}$ M$_\odot$ galaxies.

Using this, what we find is that the massive galaxy density is roughly constant and similar to its value at $z \sim 0$ up to $z = 1.5$, with a decline thereafter. There is then a real decline at higher redshifts, such that the number density for these massive galaxies grows by a factor of 8 between $z = 3$ and 1.5. We find this is the case for both selection methods for these massive galaxies. This demonstrates that this epoch between $z = 1.5$ and 3 is when a large fraction of massive galaxies become massive, and thus physical processes are ongoing during this epoch which produces this increase of almost a factor of 10 in the number of massive galaxies with $M_* > 10^{11}$ M$_\odot$ during this relatively short period of ∼2 Gyr. Future GNS papers will address the physical mechanisms which are producing this evolution.

5 SUMMARY

The GNS is a 180-orbit *HST* programme designed to obtain deep NICMOS H_{160}-band imaging of over 80 massive $>10^{11}$ M$_\odot$ galaxies at $1.7 < z < 2.9$. The depths reached are $H_{160} \sim 26.8$ AB mag (5σ), allowing for a range of other science questions to be addressed, including examining the lower mass galaxy population present within the same fields and redshifts. In this paper, we describe the GNS survey and give information about its field selection, as well as a description of the types of galaxies we initially select for field placement, and how this compares to a newer *BVizH* photometric redshift selection based on the combination of H_{160} band and ACS data. We utilize only these five filters so as to have a high fidelity in our photometry quality, depth and resolution. Our photometric redshifts are in fact very good, with a typical $\delta z/(1+z) \sim 0.1$.

We also examine in this paper ways to select massive galaxies at high redshift $z > 2$ in the absence of a significant number of spectroscopic redshifts. A very popular method for determining a galaxy population at $z > 2$ is through the use of various colour cuts e.g. BzK galaxies, DRGs or Lyman-break galaxies. We find overall that no single colour criterion is able to account for all massive galaxies and that there is considerable overlap between the various methods, many of which find the same galaxies. Overall, we find that the BzK, DRG and IERO overlap, with over 50 per cent between any two types. IEROs are the type which most overlaps the other two and perhaps provides the most complete sample of at least the red galaxies selected at higher redshifts.

We show that a photometric redshift selection with a strict narrow redshift and stellar mass range gives slightly different galaxy populations than the cumulative colour selection. In particular, we find that there are more blue massive galaxies at $z > 2$ than what is found through the standard colour cuts. Galaxies absent from each of these bins are missed as they are just outside the stringent mass and redshift-selection criteria we have imposed. A similar issue is present for the colour selection of high-z galaxies – there is always a population just outside a colour selection that has intrinsic properties nearly identical to the galaxies within the original colour-based selection. This is especially the case if one considers galaxies selected by stellar mass and redshift. We find, however, that this is not a significant limitation as we obtain the same number densities and average properties using a colour selection and a photometric redshift selection.

We also provide a summary of our understanding of how these massive galaxies evolve at high redshifts and how they are connected to lower redshift massive galaxies. Our conclusions regarding an analysis of the massive galaxy population reveal that major mergers are not adequate for driving the evolution of massive galaxies at $z < 3$ (Bluck et al. 2009). Our conclusions based on an examination of the major merger rate at $z \sim 2$–3 (Bluck et al. 2009), and the star formation properties (Weinzirl et al., in preparation) of the massive galaxies, suggests that other mechanisms, such as minor mergers and/or gas accretion and subsequent star formation are also needed to produce the increase in stellar mass within these galaxies over time. Furthermore, the 'discy' nature of a large fraction of the massive galaxies at $z \sim 2$–3, and their star formation properties (Weinzirl et al., in preparation), raises questions on the importance of major mergers in building up such systems at $z > 3$.

We find that even at $z \sim 2.5$, there is a broad colour–magnitude bimodality in galaxies, such that the massive systems are nearly always red and luminous, while lower mass galaxies tend to be much bluer. The build-up of the red sequence at $z > 2.5$ is further investigated in Grützbach et al. (2011a).

We are also investigating various other properties of these massive galaxies, including the AGN content and how AGN in massive galaxies evolves through time (Bluck et al. 2011; Weinzirl et al., in preparation), including how much energy the AGN inputs into the galaxy while it is evolving. Details of these calculations will be

presented in future GNS papers utilizing the data from this paper as well as data from other space and ground-based telescopes, such as *Spitzer* and *Chandra*.

In the future, to make progress with massive galaxy evolution in the redshift range $z > 2$ will require either a very large number of reliable photometric redshifts, that are studied in a statistical sense, or ultimately through spectroscopic surveys that will acquire redshifts and other physical information for distant massive galaxies. This should be possible with multiobject NIR spectroscopy which is now becoming feasible with new instrumentation on 8–10 m class telescopes. Probing massive galaxy formation at higher redshifts will require even larger telescopes and instruments and will likely be a major focus of *James Webb Space Telescope* (*JWST*) and the TMT/ELT/GMT era.

ACKNOWLEDGMENTS

The data and catalogues as used in the GNS survey are online at http://www.nottingham.ac.uk/astronomy/gns/. We thank Will Hartley for providing diagnostic lines of stellar populations and Omar Almaini for discussions on various aspects of this analysis. We thank STFC for support through studentships and PDRA funding. Support was also provided by NASA/STScI grant HST-GO11082. SJ and TW acknowledge support from the National Aeronautics and Space Administration (NASA) LTSA grant NAG5-13063, NSF grant AST-0607748 and HST grant GO-11082 from STScI, which is operated by AURA, Inc., for NASA, under NAS5-26555.

REFERENCES

Balestra I. et al., 2010, A&A, 512, 12
Barger A. et al., 2008, ApJ, 689, 687
Bauer A. E. et al., 2011, MNRAS, submitted
Beckwith S. et al., 2006, AJ, 132, 1729
Benitez N., 2000, ApJ, 536, 571
Bergeron L., Dickinson M., 2003, Internal STScI Report
Bluck A. F. L., Conselice C. J., Bouwens R. J., Daddi E., Dickinson M., Papovich C., Yan H., 2009, MNRAS, 394, L51
Bluck A. F. L., Conselice C. J., Almaini O., Laird E. S., Nandra K., Grützbauch R., 2011, MNRAS, 410, 1174
Bohlin R. C., Mack J., Hartig G., Sirianni M., 2005, Instrument Science Report ACS, 2005-12
Bolzonella M. et al., 2000, A&A, 363, 476
Bouwens R. J., Illingworth G. D., Franx M., Ford H., 2007, ApJ, 670, 928
Bouwens R. J. et al., 2009, ApJ, 705, 936
Bouwens R. et al., 2010, ApJ, 725, 1587
Bruzual G., Charlot S., 2003, MNRAS, 344, 1000 (BC03)
Buitrago F., Trujillo I., Conselice C. J., Bouwens R. J., Dickinson M., Yan H., 2008, ApJ, 687, L61
Bundy K. et al., 2006, ApJ, 651, 120
Bundy K. et al., 2008, ApJ, 681, 931
Calzetti D. et al., 2000, ApJ, 533, 682
Casey C. M., Chapman S. C., Muxlow T. W. B., Beswick R. J., Alexander D. M., Conselice C. J., 2009, MNRAS, 395, 1249
Cassata P. et al., 2010, ApJ, 714, 79
Conselice C. J., Bershady M. A., Dickinson M., Papovich C., 2003, AJ, 126, 1183
Conselice C. J., Bundy K., Ellis R. S., Brichmann J., Vogt N. P., Philips A. C., 2005, ApJ, 628, 160
Conselice C. J. et al., 2007a, MNRAS, 381, 962
Conselice C. J. et al., 2007b, ApJ, 660, L55
Conselice C. J., Bundy K., U V., Eisenhardt P., Lotz J., Newman J., 2008a, MNRAS, 383, 1366
Conselice C. J., Rajgor S., Myers R., 2008b, MNRAS, 386, 909
Conselice C. J., Yang C., Bluck A., 2009, MNRAS, 394, 1956
Daddi E. et al., 2004, ApJ, 617, 746
Daddi E. et al., 2007, ApJ, 670, 156
Davis M. et al., 2007, ApJ, 660, L1
de Jong R. S. et al., 2006, Instrument Science Report NICMOS 2006-003
Dickinson M. et al., 2000, ApJ, 531, 624
Dickinson M. et al., 2004, ApJ, 600, L99
Faber S. M. et al., 2007, ApJ, 665, 265
Finkelstein S. L., Papovich C., Giavalisco M., Reddy N. A., Ferguson H. C., Koekemoer A. M., Dickinson M., 2010, ApJ, 719, 1250
Foucaud S., Conselice C. J., Hartley W. G., Lane K. P., Bamford S. P., Almaini O., Bundy K., 2010, MNRAS, 406, 147
Franx M. et al., 2003, ApJ, 587, L79
Giavalisco M. et al., 2004, ApJ, 600, L93
Grazian A. et al., 2007, A&A, 465, 393
Greve T. R., Pope A., Scott D., Ivison R. J., Borys C., Conselice C. J., Bertoldi F., 2008, MNRAS, 389, 1489
Grützbauch R., Conselice C. J., Varela J., Bundy K., Cooper M. C., Skibba R., Willmer C. N. A., 2011a, MNRAS, 411, 929
Grützbauch R. et al., 2011b, MNRAS, in press (arXiv:1011.4846, doi:10.1111/j.1365-2966.2010.18060.x)
Guhathakurta P., Tyson J. A., Majewski S. R., 1990, ApJ, 357, L9
Jogee S. et al., 2009, ApJ, 697, 1971
Kajisawa M. et al., 2009, ApJ, 702, 1393
Kriek M. et al., 2008, ApJ, 677, 218
Lane K. et al., 2007, MNRAS, 379, L25
Le Fevre O. et al., 2005, A&A, 439, 845
Lotz J. M. et al., 2008, ApJ, 672, 177
Luo G. et al., 2008, ApJS, 179, 19
Magee D., Bouwens R., Illingworth G., 2007, in Shaw R. A., Hill F., Bell D. J., eds, ASP Conf. Ser. Vol. 376, Astronomical Data Analysis Software and Systems XVI. Astron. Soc. Pac., San Francisco, p. 261
Maraston C., 2005, MNRAS, 362, 799
Metcalfe N., Shanks T., Weilbacher P. M., McCracken H. J., Fong R., Thompson D., 2006, MNRAS, 370, 1257
Papovich C., Dickinson M., Ferguson H. C., 2001, ApJ, 559, 620
Papovich C. et al., 2006, ApJ, 640, 92
Papovich C., Finkelstein S. L., Ferguson H. C., Lotz J. M., Giavalisco M., 2010, preprint (arXiv:1007.4554)
Popesso P. et al., 2009, A&A, 494, 443
Ravindranath S. et al., 2006, ApJ, 652, 963
Reddy N. et al., 2005, ApJ, 633, 748
Reddy N., Steidel C. C., Pettini M., Adelberger K. L., Shapely A. E., Erb D. K., Dickinson M., 2008, ApJS, 175, 48
Retzlaff J. et al., 2010, A&A, 511, 50
Sawicki M., Yee H. K. C., 1998, AJ, 115, 1329
Scoville N. et al., 2007, ApJS, 172, 1
Shapley A., Steidel C. C., Adelberger K. L., Dickinson M., Giavliasco M., Pettini M., 2001, ApJ, 562, 95
Stanford S. A., Dickinson M., Postman M., Ferguson H. C., Lucas R. A., Conselice C. J., Budavari T., Somerville R., 2004, AJ, 127, 131
Steidel C. C., Hamilton D., 1992, AJ, 104, 941
Thompson R. et al., 1999, ApJ, 523, 100
Thompson R. et al., 2005, AJ, 130, 1
Trujillo I., Conselice C. J., Bundy K., Cooper M. C., Eisenhardt P., Ellis R. S., 2007, MNRAS, 382, 109
van Dokkum P. G. et al., 2009, PASP, 121, 2
Vanzella F. et al., 2008, A&A, 478, 83
Wang W.-H. et al., 2010, ApJS, 187, 251
Williams R. et al., 1996, AJ, 112, 1335
Wirth G. et al., 2004, AJ, 127, 3121
Wuyts S. et al., 2008, ApJ, 689, 653
Yan H. et al., 2004, ApJ, 616, 63
Yan H. et al., 2005, ApJ, 634, 109

This paper has been typeset from a TEX/LATEX file prepared by the author.